ORIGINAL ARTICLE

Winter "warm Arctic-cold Eurasia" pattern and its statistical linkages to oceanic precursors during the era of satellite observations

Pawel Schlichtholz[1]

Abstract

A striking recurrent feature of winter climate variability is the "warm Arctic-cold Eurasia" (WACE) pattern of opposite sign anomalies of surface air temperature (SAT) in the Barents Sea region and midlatitude Eurasia. Its origins and mechanisms are hotly debated, and its predictability remains unknown. This study investigates statistical relationships of the winter WACE dipole with concurrent anomalies of atmospheric circulation and oceanic precursors during the era of satellite observations. The results reveal a high potential for seasonal predictability of not only the WACE dipole but also several related indicators of winter climate variability, including the Arctic and Eurasian SAT anomalies. During subperiods of extreme covariability between the Arctic and Eurasian SATs around the early 1980s and late 2000s, most of the WACE variability is explained by ocean temperature and surface turbulent heat flux anomalies in the Barents Sea region during the preceding months. Anomalies in summer Atlantic water temperature (AWT) and autumnal sea surface temperature (SST) in this region explain about 70–80% of the variance of the following winter WACE variability during all events of strong Arctic-Eurasian SAT covariability. Analysis of SST variability in the Arctic-North Atlantic region suggests that the winter WACE link to the summer AWT anomalies reflects an atmospheric response to a large-scale surface reemergence of ocean temperature anomalies. However, this linkage had been robust only until the early 2000s. Since then, the winter WACE variability has been strongly related to autumnal SST anomalies in the Barents Sea region and the North Pacific.

Keywords Interannual variability · Air temperature anomalies · Barents Sea · Eurasia · Winter WACE pattern · Oceanic predictors
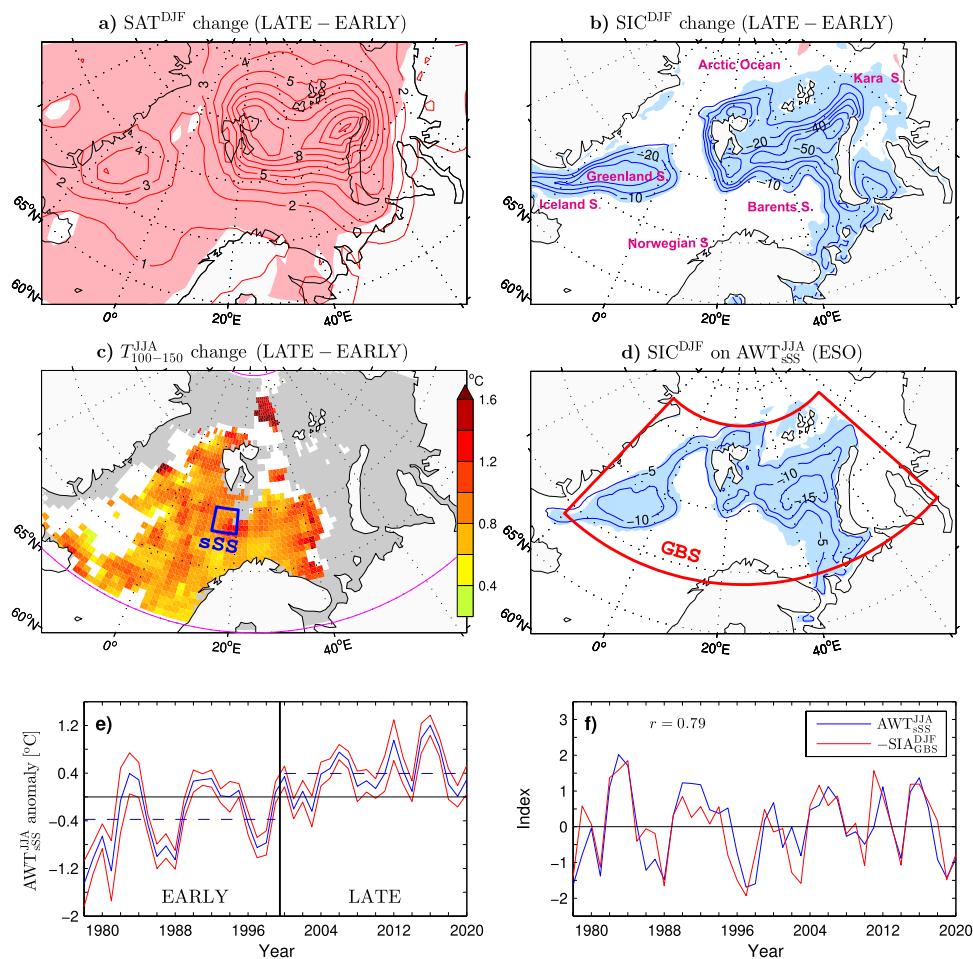
1 Introduction

During the last few decades, surface atmospheric warming has been much faster in the Arctic than globally, a phenomenon called "Arctic amplification" (Serreze and Barry 2011; Huang et al. 2017b; Rantanen et al. 2022). Although atmospheric processes contribute to this phenomenon (Bintanja et al. 2011; Pithan and Mauritsen 2014; Woods and Caballero 2016), declining Arctic sea ice may play a modulational role through enhanced upward longwave radiation and turbulent heat fluxes from the ocean to the atmosphere in the cold season (Screen and Simmonds 2010; Dai et al. 2019). In that season, Arctic warming can be driven by the "ocean heat capacitor" that discharges back into the atmosphere excess heat accumulated in the upper ocean by increased shortwave absorption in areas of summer sea ice loss (Chung et al. 2021). However, in winter, Arctic Ocean temperature is much higher than the frigid Arctic air temperature. Thus, even without the increased summertime absorption of solar radiation, the Arctic Ocean will release more heat to warm the air in winter if there is winter sea ice loss (Dai and Jenkins 2023). The recent winter Arctic warming may have resulted from the sea ice response to changes in regional (Smedsrud et al. 2013; Li et al. 2017) or large-scale (Beer et al. 2020; Shu et al. 2022) ocean heat transport, the latter possibly related to the Atlantic Multidecadal Oscillation (AMO) (Chylek et al. 2009; Fang et al. 2022). During the ice growth season, the largest Arctic sea ice decline has been observed in the Barents Sea area (Onarheim et al. 2018; Simmonds and Li 2021) where it has been accompanied by a remarkable transition to warmer ocean conditions (Årthun et al. 2012; Alexeev et al. 2013; Polyakov et al. 2017; Lind et al. 2018; Schlichtholz 2019; Skagseth et al. 2020).

✉ Pawel Schlichtholz
schlicht@iopan.gda.pl

1 Institute of Oceanology, Polish Academy of Sciences, Powstancow Warszawy 55, 81-712 Sopot, Poland

a) SAT^{DJF} change (LATE − EARLY)

b) SIC^{DJF} change (LATE − EARLY)

c) $T_{100-150}^{JJA}$ change (LATE − EARLY)

d) SIC^{DJF} on AWT$_{sSS}^{JJA}$ (ESO)

e)

f)

Fig. 1 **a** Difference of winter surface air temperature (SAT) in the Greenland–Barents Seas region between the LATE (2000–2020) and EARLY (1978–1999) epochs of the ESO period [contour interval (CI) = 1 K]. **b** As in **a** but for sea ice concentration (SIC, CI = 10%). **c** As in **a** but for summer ocean temperature north of 65°N averaged over the 100–150 m depth layer. Areas of insufficient data (see Sect. 2.2) or shallower than 100 m are grey-shaded. Temperature differences nonsignificant at $p = 0.05$ are masked in white. **d** As in **b** but for winter SIC anomalies (CI = 5% SD^{-1}) regressed onto the preceding summer AWT$_{sSS}$ index (blue curve in **f**). **e** Time series of (blue) summer anomalies of AWT$_{sSS}$ (Atlantic water temperature averaged over the 100–300 m depth layer and the sSS box in **c**, 73°–75°N, 13°–20°E) and (red) their 95% confidence limits. Dashed lines show the mean values over the EARLY and LATE epochs. **f** Standardised detrended time series of (blue) the summer AWT$_{sSS}$ index and (red) the following winter anomalies of SIA$_{GBS}$ (SIC integrated over the GBS box in **d**) with sign reversed. In **a**, **b**, and **d**, red (resp. blue) contours are for positive (resp. negative) anomalies. Red (resp. blue) shading marks positive (resp. negative) anomalies significant at $p = 0.05$

These changes are illustrated in Fig. 1a–c showing the differences in winter surface air temperature (SAT), winter sea ice concentration (SIC), and summer subsurface ocean temperature between the LATE (2000–2020) and EARLY (1978–1999) epochs of the era of satellite observations (ESO), respectively.

Arctic amplification has recently attracted great attention due not only to dramatic changes in the Arctic climate system and its ecological and economic implications for the region (Meier et al. 2014) but also to its potential influences on extreme weather events, climatic anomalies, and trends across midlatitude continents (Overland et al. 2011; Cohen et al. 2014, 2020; Dai and Song 2020; Rudeva and Simmonds 2021; Zhuo et al. 2023). A striking feature of Arctic-midlatitude linkages in winter is a SAT anomaly pattern in which warming in the Barents Sea region coexists with cooling over midlatitude Eurasia. This dipole is often called the "warm Arctic-cold Eurasia" (WACE) pattern (Mori et al. 2014) or, in its opposite phase, the "cold Arctic-warm Eurasia" (CAWE) pattern (Kim et al. 2021). The WACE dipole is a recurrent mode of climate variability on various timescales, from subseasonal (Kug et al. 2015; Luo et al. 2016; Tyrlis et al. 2020) to interannual (Mori et al. 2019; Wang et al. 2020) and multidecadal (Jin et al. 2020; Chen et al. 2021; Luo et al. 2022a). It has not only different preferential areas of occurrence but also distinct physical

characteristics compared to the well-known Greenland-Eurasian thermal seesaw driven by the North Atlantic Oscillation (NAO) or the Arctic Oscillation (Mori et al. 2014; Kim and Son 2016; Ye and Messori 2020). The winter WACE pattern may be driven by autumnal sea ice decrease in the Eurasian Arctic (Honda et al. 2009; Kim and Son 2020; Zhang and Screen 2021) through a stratospheric pathway (Kim et al. 2014; Zhang et al. 2018) or a tropospheric pathway that involves atmosphere-ice-ocean feedbacks (Jang et al. 2021). It may also be driven by the concurrent sea ice decrease in the Barents Sea area (Petoukhov and Semenov 2010; Inoue et al. 2012; Mori et al. 2014, 2019; Luo et al. 2016; Kug et al. 2015; Wang et al. 2020), which creates conditions favourable to an intensification or expansion of the Siberian High through changing pathways of high-latitude cyclones (Inoue et al. 2012) or more frequent Eurasian blocking situations (Mori et al. 2014), especially over the Ural Mountains (Luo et al. 2016, 2017c, 2019b; Yao et al. 2017; Dai and Deng 2022). However, the Arctic-Eurasian linkages are nonlinear (Petoukhov and Semenov 2010), obfuscated by the chaotic nature of extratropical circulation (Overland et al. 2021), and mingled with teleconnections to remote forcings from the North Atlantic (Sato et al. 2014; Jung et al. 2017; Luo et al. 2019a; Li et al. 2021) and the Pacific Ocean (Matsumura and Kosaka 2019; Luo et al. 2021, 2023; Zhao et al. 2022). Whether and to what extent SIC anomalies in the Eurasian Arctic influence air temperature variability over midlatitude Eurasia is uncertain (Blackport et al. 2019; Xu et al. 2019; Zhao et al. 2023).

An important fact about the variability of winter sea ice cover in the Barents Sea area is that it is closely related to anomalies of Atlantic water temperature (AWT) advected by ocean currents from the south (Helland-Hansen and Nansen 1909; Furevik 2001; Nakanowatari et al. 2014) or driven locally by air-sea interactions in late winter (Schlichtholz and Houssais 2011; Herbaut et al. 2015). These interactions influence sea ice formation during the following cold season through another kind of "ocean heat capacitor" mechanism, namely the reemergence of sea surface temperature (SST) anomalies (Schlichtholz 2011, 2021; Bushuk et al. 2017, 2019). This mechanism refers to temperature anomalies stored in the deep surface mixed layer at the end of winter, then shielded from the surface by the summer seasonal pycnocline, and subsequently reentrained into the deepening mixed layer during the cooling season (Deser et al. 2003). An index of the observed summer AWT variability in the Barents Sea opening introduced in previous studies (Schlichtholz 2019, 2021) and here extended to cover the ESO period from 1978 to 2020 (see Sect. 2.2) explains 79% of the following winter variance of the observed sea ice area (SIA) in the Greenland–Barents Seas (GBS) region (red box in Fig. 1d) and 62% of the corresponding variance when the linear trend is removed from the data (see Fig. 1f for

the detrended time series). Not all of such a strong lead-lag covariability does necessarily reflect a direct physical cause-and-effect relationship but can partly reflect local climate feedbacks that amplify and make persistent the wintertime anomalies (Schlichtholz 2013; Deng and Dai 2022). Since, on the one hand, the wintertime SIC anomalies in the Eurasian Arctic are strongly linked to earlier AWT anomalies and, on the other hand, they likely influence the Eurasian climate variability, elements of this variability that are most affected by the sea ice changes could, to some extent, be predictable. One study reported significant links of winter tropospheric circulation over Eurasia to summer ocean temperature anomalies in the Barents Sea (Schlichtholz 2016). However, that study covered only the period 1982–2005. Therefore, it remains an open question whether or not linkages of winter Eurasian climate variability in general and the WACE pattern in particular to ocean thermal conditions in the Barents Sea region have recently changed. The present study aims to address this question through lead-lag regression analysis performed for the entire ESO period, its EARLY and LATE epochs, and moving window subperiods using linearly detrended ocean observational data and atmospheric reanalysis.

Given the complexity of the Arctic-midlatitude linkages, the WACE pattern may not be robustly related to a single precursor. Therefore, the WACE relation to the AWT anomalies in the Barents Sea is compared to its relation to other potential predictors. These predictors include specific indices based on monthly or seasonal regression patterns of SST, SIC, and surface turbulent heat flux in the Arctic and SST in the North Atlantic and Pacific Oceans, as well as standard oceanic indices, such as SST-based indices of the Pacific Decadal Oscillation (PDO), El Niño, and AMO. Some of the selected predictors are closely related in time (with up to a few seasons difference), whereas other are mainly low-frequency factors (e.g., AMO and PDO) that may form a slowly-changing background (Gu and Gervais 2021) upon which the "higher frequency" interactions are taking place. Other predictands, such as SAT anomalies over the Arctic and Eurasian lobes of the WACE pattern and indices of WACE-related anomalies of sea level pressure (SLP) and upper tropospheric circulation, are also analysed. We will show, for the first time, a strong relation of the WACE pattern to its potential predictors and a systematic change of the impact of the key ones (decreasing influence of some and increasing influence of others) through the ESO period. A potentially high predictability of the WACE variability and related climatic anomalies will be demonstrated using a multiple linear regression (MLR) model.

The study is organised as follows. An outline of the data and methods is given in Sect. 2. The winter WACE dipole and its links to the concurrent anomalies of sea ice cover in the Eurasian Arctic, large-scale atmospheric circulation,

and quasi-stationary planetary waves are investigated in Sect. 3. Links to oceanic conditions in the Arctic and large-scale SST anomalies in the preceding seasons are studied in Sect. 4. The results from the MLR model are presented in Sect. 5. A summary and conclusions follow in Sect. 6.

2 Data and methods

2.1 Atmospheric, sea ice, and sea surface temperature data

Seasonal mean atmospheric variables for winter (December–January–February, DJF) and other seasons during the ESO period (1978–2020, years of December) are constructed using monthly fields from the National Centers for Environmental Prediction/National Center for Atmospheric Research (NCEP/NCAR) reanalysis (Kalnay et al. 1996, https://psl.noaa.gov/data/gridded/data.ncep.reanalysis.html). SAT, SLP, and fields at constant pressure levels, including air temperature (T), geopotential height (Z), and zonal wind velocity (u, positive eastward) are provided on a 2.5° latitude × 2.5° longitude horizontal grid. Other fields, including the zonal and meridional components of surface (10-m) wind velocity ($\mathbf{u}_s$), 2-m air temperature (T_s), and components of the total surface heat flux (Q_{total}) are provided on a ∼ 2° latitude × ∼ 2° longitude grid. The components of Q_{total} (positive upward) include the net longwave (Q_{LW}) and shortwave (Q_{SW}) radiation fluxes and the sensible (Q_{SH}) and latent (Q_{LH}) heat fluxes. The sensible and latent fluxes are summed to obtain the total turbulent heat flux (THF = $Q_{\text{SH}} + Q_{\text{LH}}$). In addition to the net radiation fluxes, the upward ($^{\uparrow}Q_{\text{LW}}$) and downward ($^{\downarrow}Q_{\text{LW}}$) contributions to Q_{LW} and the upward contribution to Q_{SW} ($^{\uparrow}Q_{\text{SW}}$) are analysed. The components of $\mathbf{u}_s$ are used to compute the surface wind curl (SWC = $\mathbf{k} \cdot \boldsymbol{\nabla}_h \times \mathbf{u}_s$, where $\boldsymbol{\nabla}_h$ is the horizontal gradient operator, and $\mathbf{k}$ denotes a vertical unit vector). They are also used to calculate SAT advection by the horizontal wind ($-\mathbf{u}_s \cdot \boldsymbol{\nabla}_h T_s$) and the contribution to this advection from the anomalous wind ($-\mathbf{u}'_s \cdot \boldsymbol{\nabla}_h T_s$, where the prime refers to the anomaly from the mean over the analysed period). Quasi-stationary Rossby waves are analysed using the zonally asymmetric component of the geopotential height at 300 hPa (Z^*_{300}).

For comparison of surface temperature anomalies, the gridded (1° latitude × 1° longitude) monthly mean Berkeley Earth Land/Ocean Temperature (LOT) dataset with air temperatures at sea ice locations interpolated using land air temperatures (Rohde and Hausfather 2020, https://berkeleyearth.org/data) is used. The monthly NAO index, obtained from the National Oceanic and Atmospheric Administration (NOAA) Climate Prediction Center (https://www.cpc.

ncep.noaa.gov/products/precip/CWlink/pna/nao.shtml), is based on 500-hPa geopotential height anomalies poleward of 20°N (Barnston and Livezey 1987).

The Arctic sea ice variables, including the SIC change from the EARLY to the LATE epoch in Fig. 1b, are calculated from monthly mean SIC data based on bootstrapped satellite observations and provided on a 25 × 25 km grid by NOAA's National Snow and Ice Data Center (NSIDC) (Comiso 2017, https://nsidc.org/data/nsidc-0079). SST variables are based on monthly data on a 1° latitude × 1° longitude grid from the NOAA Optimum Interpolation (OI) SST V2 dataset derived from remote and in situ observations (Reynolds et al. 2002, https://psl.noaa.gov/data/gridded/data.noaa.oisst.v2.html). Since these SST data are available only since December 1981, they are extended back to February 1978 using the monthly Extended Reconstructed SST V5 dataset (Huang et al. 2017a, https://psl.noaa.gov/data/gridded/data.noaa.ersst.v5.html). Standard monthly indices of SST variability, such as the PDO index, the NINO3 index of El Niño, and the unsmoothed AMO index, are taken from NOAA's Earth System Research Laboratory (https://psl.noaa.gov/gcos_wgsp/Timeseries/).

2.2 Subsurface ocean temperature data

The index of summer variability in subsurface ocean temperature (AWT_{sSS}) is defined as the June-July-August (JJA) mean anomaly of AWT averaged vertically over the 100–300 m depth layer and horizontally over the southern Svalbard slope (sSS box in Fig. 1c). This index was constructed in an earlier study for the period 1981–2017 (Schlichtholz 2019) using scattered temperature profiles from the Unified Database for Arctic and Subarctic Hydrography (UDASH) (Behrendt et al. 2018), hydrographic database of the International Council for the Exploration of the Sea (ICES) (ICES 2021), and ARctic EXperiment (AREX) database of the Institute of Oceanology, Sopot, Poland (Walczowski et al. 2017). Here, UDASH data from 1980 and ICES data from 1978, 1979, and 2018–2020 are used for the index extension. Due to the sparsity of in situ oceanic measurements and large horizontal gradients of ocean temperature in the Barents Seas region, it is a difficult task to construct a complete and reliable time series of the year-to-year subsurface ocean temperature variability in this region for the entire period under study. There are only a very few locations in the region (clustered in and around the Barents Sea opening) for which such a series can be constructed. Among these locations, the sSS area is the one for which the summer AWT anomalies are most significantly related to the following winter sea ice cover in the Barents Sea (Schlichtholz 2021). This feature likely reflects the fact that the summer AWT variability in the northern part of the Barents Sea opening to a large extent represents AWT anomalies that

are generated within the Barents Sea during the preceding seasons (Schlichtholz and Houssais 2011) and then partly outflow towards the sSS area via a westward recirculation (Skagseth 2008). In contrast, the summer AWT anomalies inflowing to the Barents Sea through the southern part of the Barents Sea opening can include independent upstream contributions and may not reach the ice edge by the following winter because the flushing time of Atlantic water in the southern Barents Sea is about 1 year (Smedsrud et al. 2010).

The AWT_{sSS} anomalies are calculated using the departures of the vertically averaged temperature at individual hydrographic stations (T_i) from a climatological temperature (T_c). The latter is obtained by horizontal averaging of the vertically averaged temperature over the selected depth layer at all summer stations found during a reference period (1981–2003) inside a circular domain with a radius of ~ 50 km around the given station. Following a procedure outlined in the previous studies (Schlichtholz 2019, 2021), for each summer, the differences $T_d = T_i - T_c$ are then averaged over the sSS box to obtain an estimate (T_m) of the AWT_{sSS} anomaly. The time series of the AWT_{sSS} anomaly (shifted to have a zero mean over the ESO period) and its confidence limits are shown in Fig. 1e. The confidence limits are defined as $T_m \pm t_c s / \sqrt{N_d}$, where s is the standard deviation (SD) of the observations (T_d values within the sSS box for the given summer), N_d is the number of the observations (ranging from 8 to 128, with the median of 36), and t_c is the critical value of the t-distribution with $N_d - 1$ degrees of freedom for the 95% confidence level.

The T_d anomalies are also computed over a broader area of the GBS region north of 65°N (southern limit of the UDASH domain) for the layers 100–150 m ($T_{100-150}$) and 0–10 m (T_{0-10}) and for all basic seasons, i.e., DJF, MAM (March-April-May), JJA, and SON (September-October-November). In areas of strong wintertime ocean heat loss to the atmosphere, including the Atlantic domain of the Barents Sea, in summer, $T_{100-150}$ and T_{0-10} represent thermal anomalies below and above the seasonal pycnocline, respectively (Smedsrud et al. 2010). The local values of $T_{100-150}$ and T_{0-10} are then used to construct maps of differences in composite means, such as the map of the summer differences in $T_{100-150}$ between the LATE and EARLY epochs of the ESO period (Fig. 1c) and maps of the differences in $T_{100-150}$ and T_{0-10} between "warm" and "cold" years for all basic seasons. To this end, the T_d's for the given season in each year are interpolated onto a 0.5° latitude × 1.5° longitude grid by an inverse distance weighted averaging of the data within a radius of influence (~ 100 km) around each grid point. The warm (resp. cold) composites are based on data from years in which the summer AWT_{sSS} anomalies with respect to their mean values in the EARLY and LATE epochs (dashed lines in Fig. 1e) are greater (resp. smaller) than 0.5 (resp. −0.5) SD. The warm years are 1982–84, 1990–95, 1999, 2006,

2007, 2012, and 2015–17. The cold years are 1978–81, 1986–88, 1997, 1998, 2000–02, 2007, 2009, 2013, and 2018. Before averaging over the warm and cold years, local mean values in the EARLY and LATE epochs are subtracted from the anomalies of $T_{100-150}$ and T_{0-10}. The sample size of the composites varies in space. The composite mean differences are calculated for the grid points for which the interpolated data are available for at least three years in each composite. Their statistical significance is estimated using a two-sample t test (von Storch and Zwiers 1999).

2.3 Climate indices and statistical techniques

If not stated otherwise, the indices of climate variability and field anomalies used in this study are based on data linearly detrended over the ESO period or its subperiods. Following some other studies (Mori et al. 2014; Wang et al. 2020), a WACE index ($WACE_{PC2}$) is defined as the principal component (PC) time series of the second (unrotated) empirical orthogonal function (EOF) mode of SAT variability in the Arctic-Eurasian region. Here, this index is derived from the winter SAT data in the region 20°–90°N, 30°W–150°E (green box in Fig. 2a) during the ESO period. In the EOF analysis, the convergence of meridians is taken into account by weighting the data with the square root of the cosine of the latitude. The second EOF explains 19% of the interannual SAT variance in the analysis domain and, according to the North's test (North et al. 1982), is independent of other EOF modes since its eigenvalue is well separated from the eigenvalues of the first and third modes, explaining 34% and 9% of the variance, respectively. In addition to $WACE_{PC2}$ and the standard indices (NAO, AMO, PDO, and NINO3), several indices are constructed by averaging data over selected areas. Some indices are defined as the standardised difference between standardised area-averaged data over regions in which the anomalies of a given variable tend to be of opposite sign. Standarisation is made by subtracting the mean and then dividing by SD. In particular, an alternative WACE index ($WACE_A$) is defined as the difference between the SAT anomalies averaged over the Arctic and Eurasian lobes of the $WACE_{PC2}$-related SAT anomaly pattern (blue and red boxes in Fig. 2a).

Linear regression analysis is used to investigate associations between spatiotemporal fields and climate indices. The linear correlation coefficient (r) between selected indices is computed for the predefined periods (ESO, EARLY, and LATE) and, in the case of some indices, also for moving windows. Moving-window correlations, denoted as r_9 and r_{15}, are computed for 9-year and 15-year windows, respectively. A specific window is referred to by giving its central year and the time span in years, e.g., 1982 ± 4 for the window covering the first 9-year-long subperiod (1978–1986). The statistical significance (p value) of the correlation
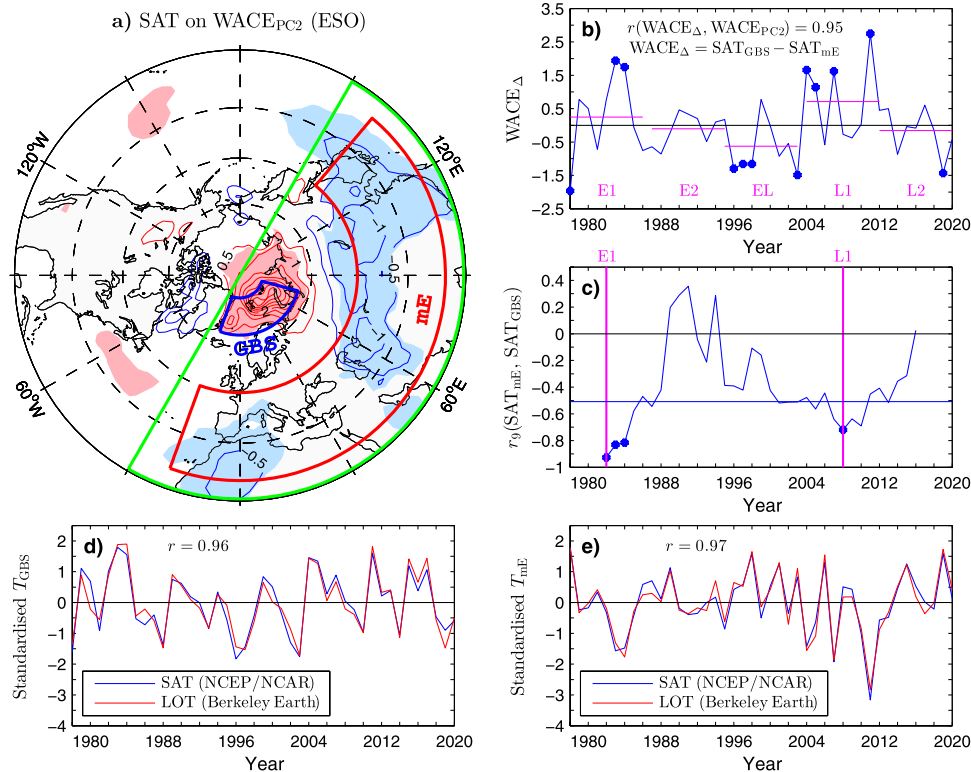
Fig. 2 **a** Winter SAT anomalies in the Northern Hemisphere extratropics (shaded if significant at $p = 0.05$, CI = 0.5 K SD^{-1}) regressed onto the concurrent WACE$_{PC2}$ index [standardised temporal coefficients of the second EOF mode of SAT anomalies in the Arctic-Eurasian sector (green box) during the ESO period]. **b** Standardised time series of the winter WACE$_{\Delta}$ index (difference of the standardised SAT$_{GBS}$ and SAT$_{mE}$ indices representing SAT anomalies averaged over the GBS and mE boxes in **a**, respectively) and its averages over subperiods E1, E2, EL, L1, and L2 (magenta lines). Blue dots mark the values in the years with strong events ($|$WACE$_{\Delta}| > 1$). Each year on the horizontal axis includes December of the DJF season. **c** 9-year

moving window correlation of the winter SAT$_{mE}$ index with the concurrent SAT$_{GBS}$ index (based on data detrended over the window and plotted at the window's central year). Blue dots mark correlations significant at $p = 0.05$. The blue horizontal line indicates the corresponding correlation for the entire ESO period. **d** Standardised time series of (blue) the SAT$_{GBS}$ index computed from the NCEP/NCAR reanalysis and (red) Land/Ocean Temperature (LOT) anomalies from the Berkeley Earth record averaged over the same area (GBS box in **a**). **e** As in **d** but for temperatures averaged over the mE box in **a**. In **a**, **b**, **d**, and **e**, the plots are based on data detrended over the ESO period

coefficients is determined by a two-tailed Student's t-test performed with an effective sample size, which is computed using the lag-1 autocorrelation coefficients of the time series (Bretherton et al. 1999).

The potential predictability of the WACE$_{\Delta}$ index and other winter variables is assessed based on (1) an MLR model of the predictand fitted to two prescribed predictors and (2) an MLR model with a stepwise selection to detect the optimal subset of predictors from a large set of initial predictors. The stepwise selection method applied here uses forward and backward regression to determine the final model (von Storch and Zwiers 1999). A function (stepwiselm) from the MATrix LABoratory (MATLAB) Statistics Toolbox (MathWorks 2014) is used to perform the regression. At each step, the function searches for predictors to add or remove from the model based on the value of a specified criterion. The criterion used here is based on the coefficient of determination (R^2) adjusted according to the

Wherry's formula: $R^2_{Adj} = 1 - (1 - R^2)(N - 1)(N - M)^{-1}$, where N is the sample size, and M is the number of predictors in the model (Wherry 1931; Bar-Gera 2017). A given predictor is added if its addition increases R^2_{Adj} by more than 0.02 and removed if its removal decreases R^2_{Adj} by less than 0.01. To avoid statistical artifacts, any predictor for which the sign of the regression coefficient from the MLR model is not the same as the sign of its bivariate correlation with the predictand is excluded. Additionally, the p values for the estimated regression coefficients are adjusted to control for the false discovery rate (FDR) in multiple testing using the Benjamini-Hochberg procedure (Benjamini and Yekutieli 2001). Only predictors passing the FDR control at $p < 0.05$ are retained. As, in some experiments, the model is applied to short time series, it is optionally constrained to allow for not more than a prescribed maximum number of predictors (M_{max}).

The MLR model with stepwise selection of predictors is run in moving window, forward extending, and backward extending period configurations. In the forward (resp. backward) extending configuration, the model is first applied to the time series over a short subperiod at the beginning (resp. end) of the ESO period and then independently to the time series over periods successively extended by adding one following (resp. preceding) year at each time step until the entire ESO period is covered. In the moving window configuration, the overall relative importance (averaged fitting skill $\overline{S}$) of the k-th predictor from the initial set of K predictors is estimated as $\overline{S}_k = [(\sum_{j=1}^{J} \Delta R^2_{kj})/(\sum_{k'=1}^{K} \sum_{j=1}^{J} \Delta R^2_{k'j})] \times 100\%$, where ΔR^2_{kj} is the increase of R^2 at the j-th window that the k-th predictor, if selected, produces when added to the model last (set to zero for the non-selected predictors), and J is the total number of windows. For some periods in the extending period configurations, the relative fitting skill of the m-th predictor selected by the model is defined as $S_m = [\Delta R^2_m/(\sum_{m'=1}^{M} \Delta R^2_{m'})] \times 100\%$, where ΔR^2_m is the increase of R^2 produced by this predictor when added last.

3 The WACE pattern and concurrent sea ice and atmospheric variability

3.1 WACE variability

Figure 2a shows the pattern of winter SAT anomalies in the ESO period associated with the PC-based WACE index. Consistent with other EOF-derived WACE patterns (Mori et al. 2014; Wang et al. 2020; Tyrlis et al. 2020), the positive phase of this index (WACE events) is characterised by warming in the Eurasian sector of the Arctic that coexists with cooling over midlatitude Eurasia. Conversely, its negative phase corresponds to CAWE events. The Arctic lobe exhibits large SAT anomalies of up to 4.3 K per unit WACE index over the northern Barents Sea and a secondary significant centre over the Greenland Sea. The midlatitude lobe consists of moderate SAT anomalies of up to 1.4 K per unit WACE index over Asia and weaker but also significant SAT anomalies in the Western Mediterranean region. An index of SAT variability in the northern lobe (SAT_{GBS}) is computed from SATs averaged over the GBS region (blue box in Fig. 2a), and an index of SAT variability in the southern lobe (SAT_{mE}) is obtained from SATs averaged over midlatitude Eurasia from 25°N to 50°N (red box in Fig. 2a). These indices, derived from the NCEP/NCAR reanalysis, are consistent ($r > 0.95$) with the corresponding indices derived from the Berkeley Earth surface temperature record (Fig. 2d, e). In further analysis, the WACE variability is represented by the $WACE_\Delta$ index (difference between the SAT_{GBS} and SAT_{mE} indices) shown in Fig. 2b. This index is almost the

same as the PC-based index ($r = 0.95$) and explains a large fraction of the interannual SAT variability over the Arctic and Eurasian lobes of the WACE pattern. (It correlates at $|r| = 0.87$ with both SAT_{GBS} and SAT_{mE}.)

Based on $WACE_\Delta$, six strong WACE events ($WACE_\Delta > 1$ SD) and six strong CAWE events ($WACE_\Delta < -1$ SD) are identified (blue dots in Fig. 2b). The timing of these events is used to divide the ESO period into five subperiods. The first subperiod (E1) includes one strong CAWE event (in 1978) and two strong WACE events (in 1983 and 1984). It is followed by a subperiod (E2) without any strong event and then by four strong CAWE events in a subperiod (EL) bridging the EARLY and LATE epochs (in 1996, 1997, 1998, and 2003). These events precede a subperiod (L1) with four strong WACE events (in 2004, 2005, 2007, and 2011) followed by a subperiod (L2) with one strong CAWE event (in 2019). The subperiods with the strong WACE events, E1 (1982 ± 4) and L1 (2008 ± 4), correspond to significant EARLY and LATE maxima of the 9-year moving window correlation between the SAT_{GBS} and SAT_{mE} indices, respectively (Fig. 2c).

3.2 Linkages to sea ice and surface heat flux anomalies in the Eurasian Arctic

Air temperature anomalies in both lobes of the WACE pattern are significant from the surface to the tropopause level at ∼ 300 hPa. This feature is demonstrated in Fig. 3e showing the latitude-vertical distribution of the regression and correlation coefficients of the WACE index with the zonally averaged anomalies of T in the Arctic-Eurasian sector for the set of twelve (ESO12) years with the strongest WACE/CAWE events during the ESO period (dots in Fig. 2b). A remarkable surface intensification of the Arctic lobe of the WACE dipole (Fig. 3e) and a significant association of the WACE events with negative SIC anomalies in the Eurasian Arctic (Fig. 3a) suggest that Arctic sea ice loss may play an important role in changes in the WACE pattern via the variability of Ural blocking (Luo et al. 2016; Dai and Deng 2022). Consistent with this scenario, the latitude-vertical structure of air temperature anomalies associated with the SIA_{GBS} index of Arctic sea ice variability (Fig. 3f, sign reversed) is similar to the corresponding WACE-related structure (Fig. 3e), reflecting a high correlation between the WACE and SIA_{GBS} indices ($r = -0.95$ for the strong WACE/CAWE events; see Table 1 for correlations between selected winter climate indices for the ESO12 years).

Over the marginal ice zone (MIZ), as SIC decreases, more warm water is exposed to the frigid air, causing huge increases in the upward turbulent and thermal radiation fluxes. As a result, warming and moistening of the lower troposphere occurs, which then increases downward thermal radiation, leading to further sea ice decrease and air warming

Fig. 3 **a** Winter SIC anomalies in the Greenland–Barents Seas region (shaded if significant at $p = 0.05$, CI = 5% SD^{-1}) regressed onto the WACE$_\Delta$ index (blue curve in Fig. 2b). **b** As in **a** but for (thin contours) anomalies of surface turbulent (sensible + latent) heat flux (THF, positive upward, masked over land, CI = 10 W m^{-2} SD^{-1}). Thick black lines show the 15% and 90% contours of the climatological winter mean SIC. **c**, **d** As in **b** but for anomalies of upward ($^\uparrow Q_{LW}$, positive upward) and downward ($^\downarrow Q_{LW}$, positive downward) longwave radiation, respectively (CI = 2 W m^{-2} SD^{-1}). **e** As in **a** but for (thin contours) air temperature anomalies (averaged between 0°E and 120°E) along a latitude-vertical cross section (CI = 0.25 K SD^{-1}) for the ESO12 years (dots in Fig. 2b). Thick contours show the correlation coefficients (for $|r| \geq 0.6$). **f** As in **e** but for air temperature anomalies regressed onto the $-$SIA$_{GBS}$ index (red curve in Fig. 1f)
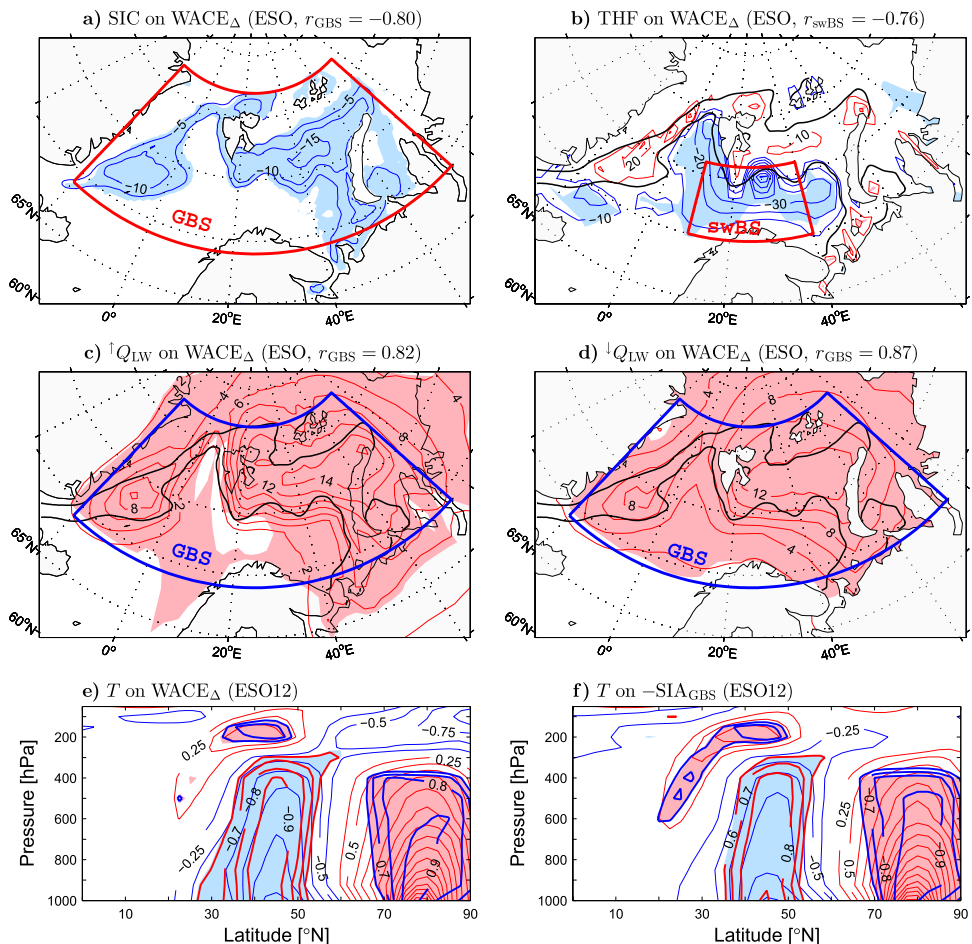
in the MIZ (Kim et al. 2019). The warm SAT anomaly may spread to nearby open water surfaces and warm the ocean by reducing upward net energy fluxes there, which further hampers the seasonal sea ice advance (Deng and Dai 2022). Such feedback loops should contribute to the WACE-related interannual Arctic climate variability given the strong WACE-SIA$_{GBS}$ linkage and the WACE-related SAT anomaly pattern, in which the largest anomalies in the GBS region appear over the areas of the largest SIC anomalies and extend significantly over nearby open water areas (Figs. 2a, 3a). However, the triggering of these loops by SIC anomalies is not evident from the perspective of simultaneous anomaly patterns of the total (not shown) or turbulent (Fig. 3b) surface heat flux. During the WACE events, the increased THFs in the MIZ are relatively weak (mostly nonsignificant) compared to strongly decreased THFs on the open water side of the ice edge. In some studies, such a structure of THF anomalies was interpreted as a signature of a minimal influence of the Barents Sea ice cover on the Eurasian climate variability (Sorokina et al. 2016; Blackport et al. 2019). According to these studies, the out-of-phase Arctic and Eurasian SAT anomalies result from a large-scale atmospheric circulation anomaly that also reduces the sea ice extent in the Barents

Sea during WACE events. However, this interpretation does not account for the complex feedbacks in the Arctic climate system. These feedbacks not only result in a strong compensation between the upward and downward thermal radiation anomalies (see Fig. 3c, d for their WACE-related regression maps) but may also involve a dynamic atmospheric response to sea ice anomalies (Deser et al. 2007), which may weaken the WACE-related THF anomalies in the MIZ. The scenario of a negligible Eurasian climate response to Arctic surface forcing is inconsistent with lagged-relationships presented in Sect. 4. In any case, the large THF anomalies on the open water side of the ice edge are a remarkable feature of the WACE-related winter Arctic climate variability. The THF$_{swBS}$ index of these anomalies (based on THFs averaged over the south-western Barents Sea, swBS box in Fig. 3b) correlates highly ($|r| > 0.90$ for the strong WACE/CAWE events) with both the WACE index and the SIA$_{GBS}$ index.

3.3 Linkages to atmospheric circulation anomalies

The relation of WACE variability to atmospheric circulation anomalies is shown in Fig. 4. Consistent with earlier studies, the most prominent feature of upper tropospheric circulation

Table 1 Selected indices of winter (DJF mean) climate variability (defined in the first four columns) and their correlation coefficient r ($\times 100$) with the concurrent $WACE_{\Delta}$ (column r_{WACE}), SIA_{GBS} (column r_{SIA}), and THF_{swBS} (column r_{THF}) indices (also defined in the table) for the winters with strong WACE/CAWE events (12 data points, dots in Fig. 2b)

| Symbol	Variable	Region	Domain/method	r_{WACE}	r_{SIA}	r_{THF}
$WACE_{\Delta}$	WACE dipole index	Arctic-Eurasia	$SAT_{GBS} - SAT_{mE}$	–	− 95	− 91
SAT_{GBS}	Surface air temperature	Greenland–Barents Seas	69°–82°N, 20°W–75°E	96	− 97	− 97
SAT_{mE}	Surface air temperature	Midlatitude Eurasia	25°–50°N, 20°W–140°E	− 96	86	78
SIA_{GBS}	Sea ice area	Greenland–Barents Seas	69°–82°N, 20°W–75°E	− 95	–	93
SST_{GBS}	Sea surface temperature	Greenland–Barents Seas	69°–82°N, 20°W–75°E	90	− 95	− 90
THF_{swBS}	Surface turbulent heat flux	South-western Barents Sea	70°–76°N, 10°–40°E	− 91	93	–
$U300_{nE}$	300-hPa zonal westerly wind	Northern Eurasia	42°–70°N, 20°–140°E	− 94	90	92
SLP_{USH}	Sea level pressure	Ural-Siberian High	35°–65°N, 20°–140°E	96	− 95	− 89
SWC_{SR}	Surface wind curl	Svalbard region	74°–85°N, 20°W–50°E	88	− 85	− 84
Z^{*}_{BKS}	300-hPa geopotential height	Barents-Kara Seas	65°–85°N, 30°–100°E	89	− 87	− 95
Z^{*}_{BA}	300-hPa geopotential height	Baffin Bay-Arctic Archipelago	65°–85°N, 150°–30°W	− 91	88	91
HWI	High-latitude wave intensity	Northern high latitudes	$Z^{*}_{BKS} - Z^{*}_{BA}$	92	− 89	− 95
Z^{*}_{mNA}	300-hPa geopotential height	Midlatitude North Atlantic	32°–53°N, 75°–10°W	66	ns	− 64
Z^{*}_{mA}	300-hPa geopotential height	Midlatitude Asia	32°–53°N, 60°–170°E	− 88	81	81
MWI	Midlatitude wave intensity	Northern mid-latitudes	$Z^{*}_{mNA} - Z^{*}_{mA}$	82	− 69	− 77
NAO	500-hPa geopotential height	Northern extratropics	Barnston and Livezey (1987)	ns	− ns	− ns

Except for the North Atlantic Oscillation (NAO) index, the selected indices are obtained by box averaging over the area given in column "Domain/method" or by subtracting the standardised values of the indices indicated in that column. THF (positive upward) is the sum of the sensible and latent heat fluxes. The correlations are computed from data detrended over the ESO period (1978–2020, years of December). Non-significant (ns) correlations at $p = 0.05$ are not given. The star in the superscript of the index symbol denotes the zonally asymmetric component of the given variable

associated with the WACE events is an anomalous anticyclone over the Barents-Kara Seas and the adjacent Ural region (see Fig. 4a for the anomalies of geopotential height at 300 hPa, Z_{300}). This anticyclone forms a dipolar structure with an anomalous cyclone over midlatitude Asia known as the "Ural blocking pattern" (Luo et al. 2016; Gong and Luo 2017). The anomalous easterlies along the common border of the northern anticyclone and the southern cyclone, with a core at ∼ 55°N and ∼ 300 hPa, correspond to a slackening of the westerly polar front jet (see Fig. 4c for the meridional distribution of the anomalies and the climatology of the zonally averaged zonal winds in the Arctic-Eurasian sector). The associated protrusions of significant positive SLP anomalies from their subpolar centre of action southward along the Urals and southeastward toward the Pacific coast correspond to an intensification and a northwestward expansion of the Siberian High (see Fig. 4b for the SLP anomalies and climatology), leading to anomalous cooling in midlatitude Asia through cold-air advection (Mori et al. 2014; Kim et al. 2021). The dependence of the WACE pattern on atmospheric circulation anomalies is summarised via correlations of the WACE index with the $U300_{nE}$ index of upper-tropospheric circulation variability and the SLP_{USH} index of surface circulation variability. These indices are defined as the zonal westerly wind anomaly at 300 hPa averaged over northern Eurasia (nE box in Fig. 4a) and the SLP anomaly averaged over an area encompassing the Urals and the Siberian High region (USH box in Fig. 4b), respectively. They correlate highly with the WACE index for all ESO years ($|r| > 0.8$) as well as during the strong WACE/CAWE events alone ($|r| \approx 0.95$).

Although the WACE variability is not significantly related to the canonical NAO index (Table 1), the WACE events are favoured by conditions in which the Ural blocking pattern occurs jointly with an upstream positive NAO-like dipole (Luo et al. 2016). This dipole consists of an equivalent-barotropic anticyclone over the North Atlantic and a baroclinic cyclone in the Arctic, centred at upper-tropospheric levels to the west and at the surface to the east of Greenland (Fig. 4a and 4b). Such conditions are favourable to increased moisture advection towards the Eurasian Arctic and subsequent surface warming in this region due to increased downward infrared radiation (Luo et al. 2017a; Gong and Luo 2017; Lee et al. 2017; Messori et al. 2018). They are also favourable to the direct generation of air temperature anomalies through anomalous temperature advection (Sato et al. 2014). In particular, warm-air advection by southwesterly-to-southerly winds on the eastern rim of the surface cyclonic circulation anomaly around Svalbard (see Fig. 4d for the anomalies of the surface wind and its curl in the GBS region) contributes to the warming over the Barents Sea (see Fig. 4e, f for the total SAT advection anomaly and

Fig. 4 **a** Winter anomalies of geopotential height at 300 hPa (Z_{300}) in the Northern Hemisphere extratropics (shaded if significant at $p = 0.05$, CI = 5 gpm SD^{-1}) regressed onto the WACE$_\Delta$ index (blue curve in Fig. 2b). **b** As in **a** but for (thin contours) anomalies of sea level pressure (SLP, CI = 0.4 hPa SD^{-1}). Thick black lines show the 1025 and 1030 hPa contours of the climatological winter mean SLP. **c** As in **a** but for (thin contours) anomalies of zonal wind (u, positive eastward, averaged between 30°E and 120°E) along a latitude-vertical cross section (CI = 0.4 m s^{-1} SD^{-1}). Thick black lines show the climatological winter mean u (CI = 6 m s^{-1}). **d** As in **a** but for (thin contours) anomalies of surface wind curl (SWC, masked over land) in the Greenland–Barents Seas region (CI = 0.4×10^{-6} s^{-1} SD^{-1}). Arrows show the corresponding anomalies of surface wind velocity (subsampled and masked if both components are nonsignificant at $p = 0.05$). Thick black lines show the 15% and 90% contours of the climatological winter mean SIC. **e**, **f** As the contours in **d** but for (thin contours) anomalies of SAT advection by the total and the anomalous horizontal wind, respectively (CI = 0.5 K day^{-1} SD^{-1})
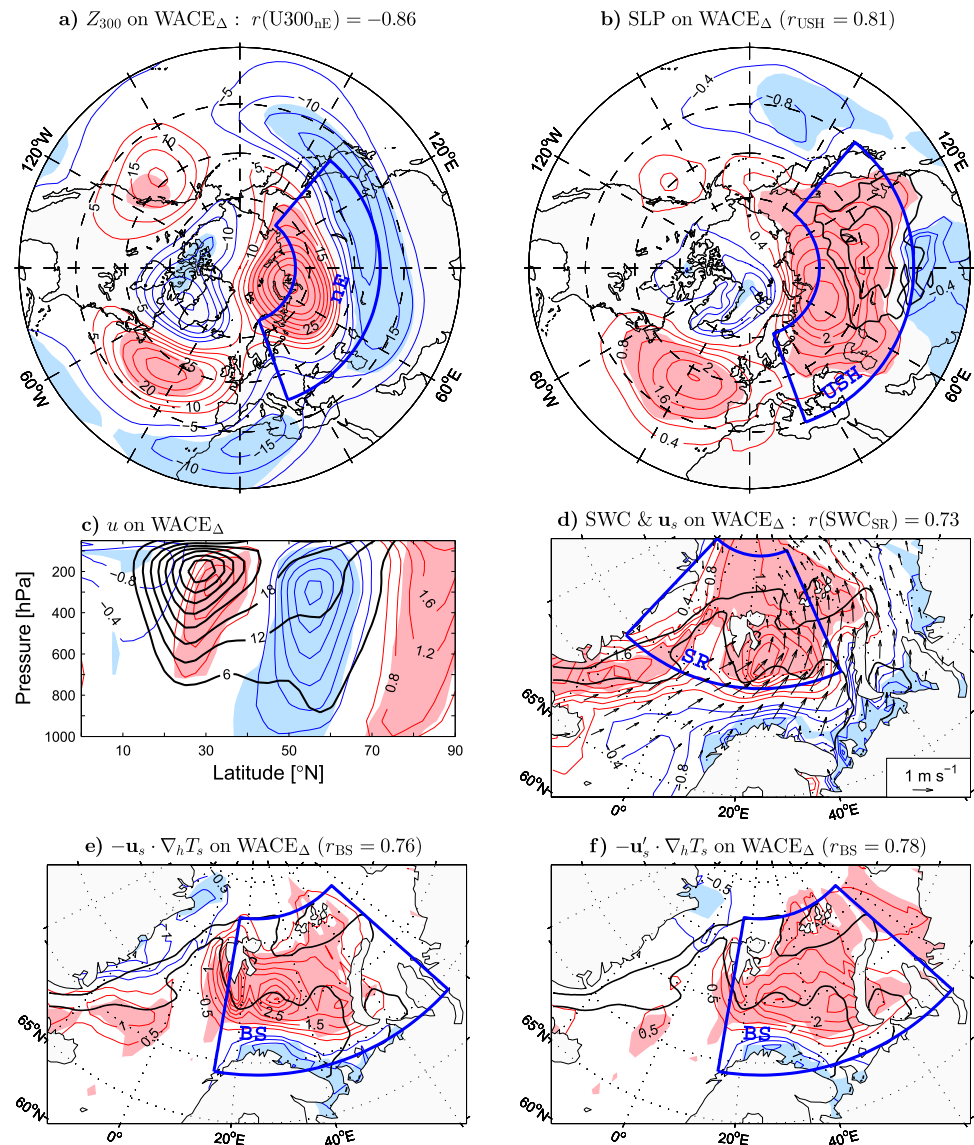
the contribution from the anomalous winds, respectively). The dynamic SAT warming (and coincident air moistening) should consequently reduce the turbulent ocean heat loss to the atmosphere on the open water side of the ice edge and dampen the anomalous ocean heat loss induced by the reduced sea ice cover (Cho and Kim 2021). Such a negative feedback may explain why the WACE-related THF anomalies in the area of large SIC variability are fairly weak (Fig. 3a, b) and makes plausible the scenario in which the WACE-related atmospheric circulation anomalies are, at least in some years, induced by surface forcing in the Arctic. In particular, Arctic sea ice loss can trigger easterly wind anomalies over northern Eurasia, which may then enhance Ural blocking activity by reducing the meridional gradient of potential vorticity (Luo et al. 2019b). In any case, during the strong WACE/CAWE events, the U300$_{nE}$ wind index is

related closely ($r \geq 0.9$) to the SIA$_{GBS}$ and THF$_{swBS}$ indices of Arctic climate variability (Table 1).

3.4 Relation to quasi-stationary planetary waves

Some studies suggest an important role of planetary waves in driving the WACE pattern (Sato et al. 2014; Yao et al. 2017). From the circumglobal perspective, the northern lobes of the Ural blocking pattern and the NAO-like dipole of the WACE-related upper-level geopotential height anomalies (Fig. 4a) can be viewed as a manifestation of a high-latitude quasi-stationary wavenumber-1 planetary wave with one lobe to the east and the other lobe to the west of the Greenwich meridian. The western lobe is barely significant in the Z_{300} anomaly pattern but prominent in the anomaly pattern of the zonally asymmetric component of Z_{300} (Fig. 5a). Similarly, the midlatitude lobes of the WACE-related anomalies
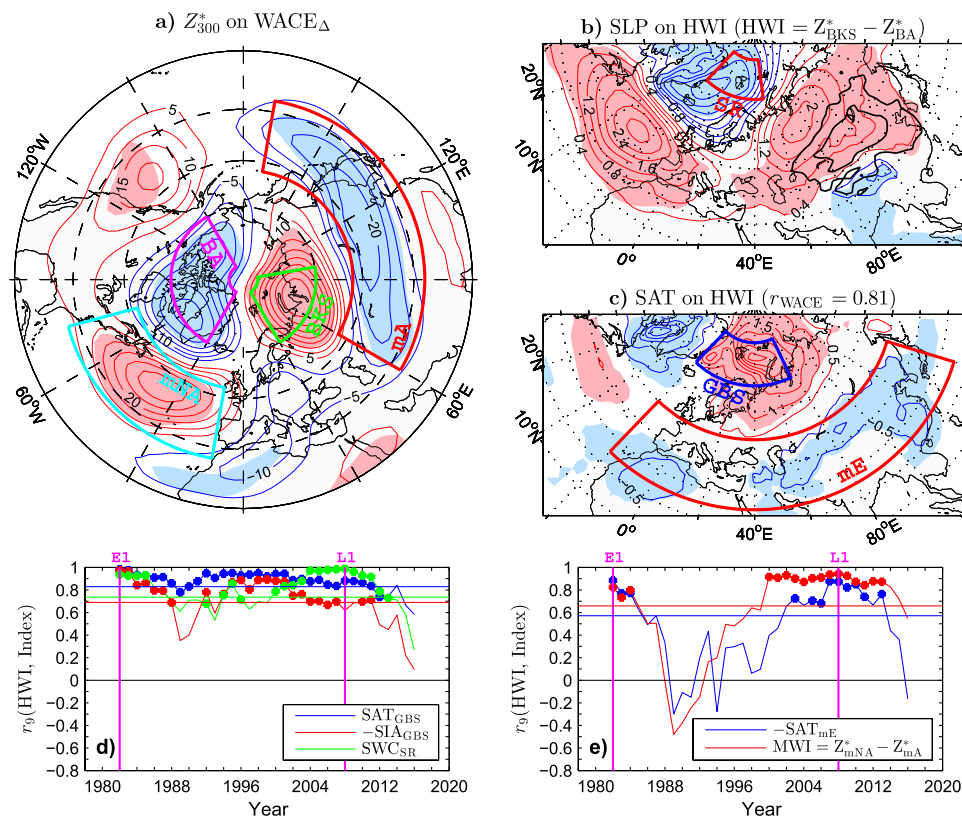
Fig. 5 a Winter anomalies of the zonally asymmetric component of Z_{300} in the Northern Hemisphere extratropics (shaded if significant at $p = 0.05$, CI = 5 gpm SD^{-1}) regressed onto the WACE$_\Delta$ index (blue curve in Fig. 2b). **b** As in **a** but for (thin contours) SLP anomalies in the Arctic-Eurasian sector (CI = 0.4 hPa SD^{-1}) regressed onto the high-latitude wave intensity (HWI) index (difference between standardised anomalies of Z_{300}^* averaged over the BKS and BA boxes in **a**). Thick black lines show the 1025 and 1030 hPa contours of the cli-

matological winter mean SLP. **c** As thin contours in **b** but for SAT anomalies (CI = 0.5 K SD^{-1}). **d** As in Fig. 2c but for correlation of HWI with (blue) the SAT$_{GBS}$ index, (red) the SIA$_{GBS}$ index (sign reversed), and (green) anomalies of surface wind curl (SWC) averaged over the SR box in **b**. **e** As in **d** but for correlation of HWI with (blue) the SAT$_{mE}$ index (sign reversed) and (red) the midlatitude wave intensity (MWI) index (difference between standardised anomalies of Z_{300}^* averaged over the mNA and mA boxes in **a**)

of Z_{300} and Z_{300}^* are reminiscent of a wavenumber-1 wave in which the western lobe is split by the North American continent into two centres of action, a major one over the North Atlantic and a minor one over the easternmost North Pacific. For further analysis, an index of the high-latitude wave intensity (HWI) is defined as the difference $Z_{BKS}^* - Z_{BA}^*$ between the anomalies of Z_{300}^* averaged over the Barents-Kara Seas and the Baffin Bay-Arctic Archipelago (BKS and BA boxes in Fig. 5a, respectively). The difference $Z_{mNA}^* - Z_{mA}^*$ between the corresponding anomalies averaged over the midlatitude North Atlantic and midlatitude Asia (mNA and mA boxes in Fig. 5a, respectively) is taken as an index of the midlatitude wave intensity (MWI).

Given a strong relation of WACE variability to the northern wave intensity ($r = 0.92$ for the ESO12 years and $r = 0.81$ for all ESO years), the HWI-related pattern of surface circulation anomalies in the Arctic-Eurasian sector (see Fig. 5b for the SLP anomaly map) is similar to the

corresponding WACE-related pattern (Fig. 4b) but exhibits a stronger Arctic lobe of low pressure anomalies. On the eastern rim of this lobe, the dynamic warming by the HWI-related surface winds should contribute efficiently to the increased Arctic SATs (Fig. 5c). Such a contribution is in accord with high values of the 9-year moving window correlation between the HWI and SAT$_{GBS}$ indices throughout the ESO period (Fig. 5d, blue curve). The overall linkage of the Eurasian SATs to the northern wave is weaker due to a pronounced quasi-decal modulation, with distinct significant maxima of $|r_9|$ at the beginning of the EARLY epoch and in the 2000s (Fig. 5e, blue curve). These maxima coincide with the maxima in covariability between the Arctic and Eurasian SATs around the E1 and L1 subperiods including all strong WACE events of the ESO period (Fig. 2b, c). This coincidence is consistent with the established influence of Ural blocking on the WACE. In particular, several studies reported a reduced persistence or frequency of Ural blocking

in the late 1980s and the 1990s compared to the preceding and subsequent years (Luo et al. 2016, 2018; Tyrlis et al. 2020).

During the subperiods of significant covariability between the Arctic and Eurasian SATs, the high-latitude planetary wave is strongly coupled to both the midlatitude wave (Fig. 5e, red curve) and surface circulation anomalies in the Arctic. The latter coupling is illustrated by the green curve in Fig. 5d showing the 9-year moving window correlation between the HWI index and an index of surface wind cyclonicity (SWC_{SR}) obtained by averaging the surface wind curl over the Svalbard region (SR box in Fig. 5b). The HWI-SWC_{SR} relationship is very strong during both the E1 ($r_9 = 0.94$) and the L1 ($r_9 = 0.99$) subperiod. As the surface cyclone appears in the vicinity of significant WACE-related SIC anomalies (Fig. 3a), this cyclone and the circumglobal wave aloft could be forced by surface conditions in the Eurasian Arctic. This scenario seems more likely in the EARLY epoch when the HWI index is highly correlated ($r_9 = -0.97$ in E1) with the SIA anomalies in the GBS region than in the LATE epoch when the HWI-SIA_{GBS} covariability is somewhat reduced (Fig. 5d, red curve). However, lagged relationships will show that atmosphere-ice-ocean interactions in the Arctic should contribute to the WACE variability also in the LATE epoch.

4 Linkages to oceanic conditions during the preceding seasons

4.1 Summer subsurface ocean temperature in the Barents Sea

4.1.1 Relations with the regional surface climate variability

The reemergence of Arctic SST anomalies is illustrated by a sequence of seasonal patterns of differences in the composite mean of ocean temperature in the subsurface ($T_{100-150}$) and surface (T_{0-10}) layers based on hydrographic observations from the GBS region (Fig. 6). The differences shown are between warm (AWT^+) and cold (AWT^-) years selected using the summer AWT_{sSS} index (see Sect. 2.2 for details and note that only significant differences are plotted). Significant positive subsurface differences in the pathways of Atlantic water through the region (marked schematically by arrows in Fig. 6e) persist from spring to the following winter (Fig. 6, left panels). In spring, the subsurface pattern (Fig. 6a) mirrors the surface pattern (Fig. 6b), reflecting local air-sea interactions leading to vertically uniform temperature anomalies in a deep surface mixed layer before seasonal stratification sets in. Over most of the region, significant surface differences disappear in summer (Fig. 6d) and, at least in the southern and central Barents Sea, reappear in
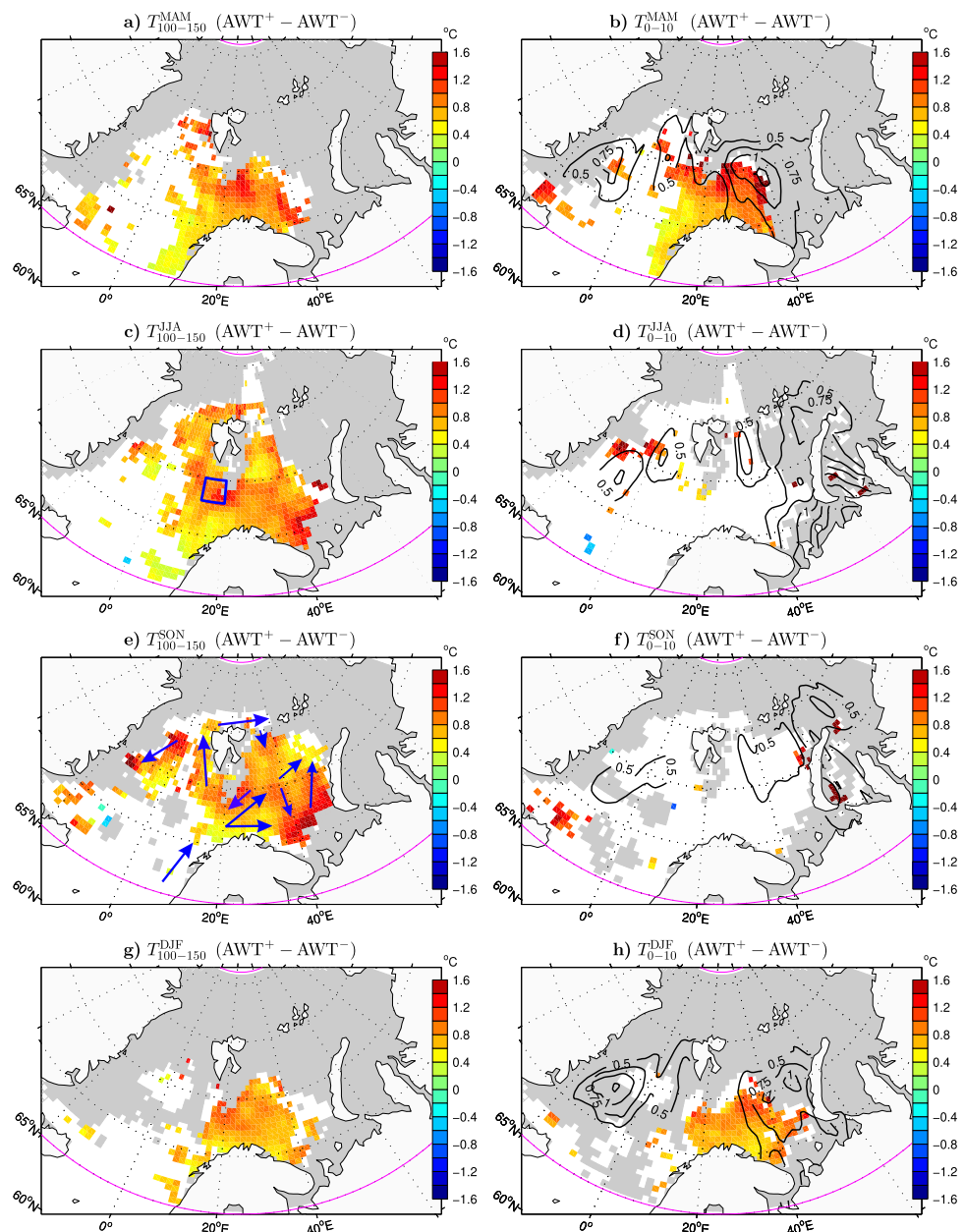
winter (Fig. 6h) when a deep surface mixed layer is formed there (Harris et al. 1998). In summer and autumn, the differences in $T_{100-150}$ in the northern Barents Sea are nearly as large as in the southern Barents Sea (Fig. 6c, e). However, in the northern Barents Sea, temperature anomalies from below the 100 m level (Atlantic water layer) cannot generally be brought to the surface via the seasonal cycle of the surface mixed layer depth because of a strong haline stratification of the Arctic water layer above, even though this stratification has recently weakened (Lind et al. 2018).

In the Greenland Sea, hydrographic observations are too scarce to demonstrate the surface reemergence of ocean heat anomalies. However, such a reemergence should also occur in this area, as indicated by the patterns of composite mean differences in the seasonal mean SST anomalies based on complete time series for each grid point and constructed in the same way as the T_{0-10} differences (black contours in Fig. 6, right panels). Similar patterns are found through regression of the seasonal mean SST anomalies onto the summer AWT_{sSS} index for all ESO years. In both the Barents and the Greenland Sea, the magnitude of the regressed winter SST anomalies (Fig. 7a) is approximately the same as the unit AWT_{sSS} index (SD = 0.46 K), suggesting that wintertime feedbacks in the regional climate system are sufficiently strong to sustain the reemerged SST anomalies through the cold season. Such feedbacks also amplify SST anomalies on longer timescales (Deng and Dai 2022; Dai and Deng 2022). In the ESO period, the summer AWT_{sSS} variability explains 72% of the following winter variance ($r = 0.85$) of SST anomalies averaged over the GBS region (SST_{GBS} index). The latter, in turn, account for 81% of the concurrent variance ($r = 0.90$) of SIA anomalies in this region (see Table 2 for correlations between selected indices of Arctic climate variability).

The importance of the subsurface ocean for surface climate variability in the Arctic is further demonstrated by time-lagged correlations of the monthly mean SST_{GBS} and SIA_{GBS} anomalies with the summer AWT_{sSS} index (see Fig. 7f and note the reversed sign of r for SIA_{GBS}). For both surface variables, the correlation shows maxima in the March preceding (lag −3 months) and the January following (lag +6 months) the summer AWT_{sSS} anomalies. After the March maximum, the correlation for SIA_{GBS} becomes nonsignificant in August and remains such until November. The correlation for SST_{GBS} remains significant through these months, but its magnitude is reduced by nearly a half in August and September, when seasonal stratification is still present in the ocean. It then increases starting from October, when subsurface ocean heat anomalies begin to be entrained into the deepening surface mixed layer. In the case of warm anomalies, above-normal temperature in the convectively mixed upper-ocean column makes cooling to the freezing point longer and enlarges the area where sea ice formation

Fig. 6 Difference in the composite mean of ocean temperature averaged over (*left*) the 100–150 m ($T_{100-150}$) and (*right*) the 0–10 m (T_{0-10}) depth layer in the Greenland–Barents Seas region north of 65°N between warm and cold years selected based on the summer AWT_{sSS} index (see Sect. 2.2) for: (**a, b**) the preceding spring, (**c, d**) the concurrent summer, (**e, f**) the following autumn, and (**g, h**) the following winter. Areas of insufficient data (see Sect. 2.2) or shallower than 100 m are grey-shaded. Temperature differences nonsignificant at $p = 0.05$ are masked in white. In the *right* panels, back contours show composite mean differences of sea surface temperature (SST) computed for the same seasons as (and similarly to) the T_{0-10} differences (CI = 0.25 K, starting at 0.5 K). In **c**, blue box shows the sSS area over which the AWT anomalies are averaged to construct the AWT_{sSS} index. In **e**, arrows depict schematically pathways of Atlantic water

a) $T_{100-150}^{MAM}$ (AWT$^+$ − AWT$^−$)   b) T_{0-10}^{MAM} (AWT$^+$ − AWT$^−$)

c) $T_{100-150}^{JJA}$ (AWT$^+$ − AWT$^−$)   d) T_{0-10}^{JJA} (AWT$^+$ − AWT$^−$)

e) $T_{100-150}^{SON}$ (AWT$^+$ − AWT$^−$)   f) T_{0-10}^{SON} (AWT$^+$ − AWT$^−$)

g) $T_{100-150}^{DJF}$ (AWT$^+$ − AWT$^−$)   h) T_{0-10}^{DJF} (AWT$^+$ − AWT$^−$)

cannot occur. The below-normal sea ice cover then leads to increased air temperature in the MIZ, as indicated by a close relation ($r = -0.95$) between the winter mean SIA anomalies in the GBS region and the concurrent SAT anomalies averaged over the GBS MIZ (taken as the area with the climatological mean SIC between 15 and 90%). A considerable fraction of the latter is explained by the preceding summer AWT_{sSS} anomalies ($r = 0.75$).

The presummer maxima in the correlation of the summer AWT_{sSS} index with both the SST_{GBS} and the SIA_{GBS} anomalies (Fig. 7f) should reflect strong atmosphere-ice-ocean interactions at the end of winter generating persistent ocean temperature anomalies. This conjecture is consistent with some studies on the origin of summertime AWT anomalies

in the Barents Sea (Schlichtholz and Houssais 2011; Bushuk et al. 2019) and supported by the anomaly pattern of the seasonal mean SAT in early spring (February-March-April, FMA) associated with the following summer AWT_{sSS} index (Fig. 7e). In this pattern, large anomalies appear in the MIZ, but significant anomalies extend also over open water. The early spring SAT anomalies and the spring SST anomalies averaged over the south-western Barents Sea (swBS box in Fig. 7e) account for a large fraction ($r = 0.81$ and $r = 0.85$, respectively) of the following summer AWT_{sSS} anomalies.

A further insight into Arctic climate variability is gained from analysis of winter surface heat fluxes associated with the preceding summer AWT_{sSS} index. During the warm phase of this index, upward THF + $^{\uparrow}Q_{LW}$ fluxes

a) SST^{DJF} on AWT^{JJA}_{sSS} ($r_{GBS} = 0.85$)

b) $(THF + {^\uparrow}Q_{LW})^{DJF}$ on AWT^{JJA}_{sSS} ($r_{GBS-MIZ} = 0.68$)

c) SWC^{DJF} & $\mathbf{u}^{DJF}_s$ on AWT^{JJA}_{sSS} : $r(SWC_{SR}) = 0.66$

d) ${^\uparrow}Q^{JJA}_{SW}$ on AWT^{JJA}_{sSS} ($r_{GBS} = -0.59$)

e) SAT^{FMA} on AWT^{JJA}_{sSS} ($r_{swBS} = 0.81$)
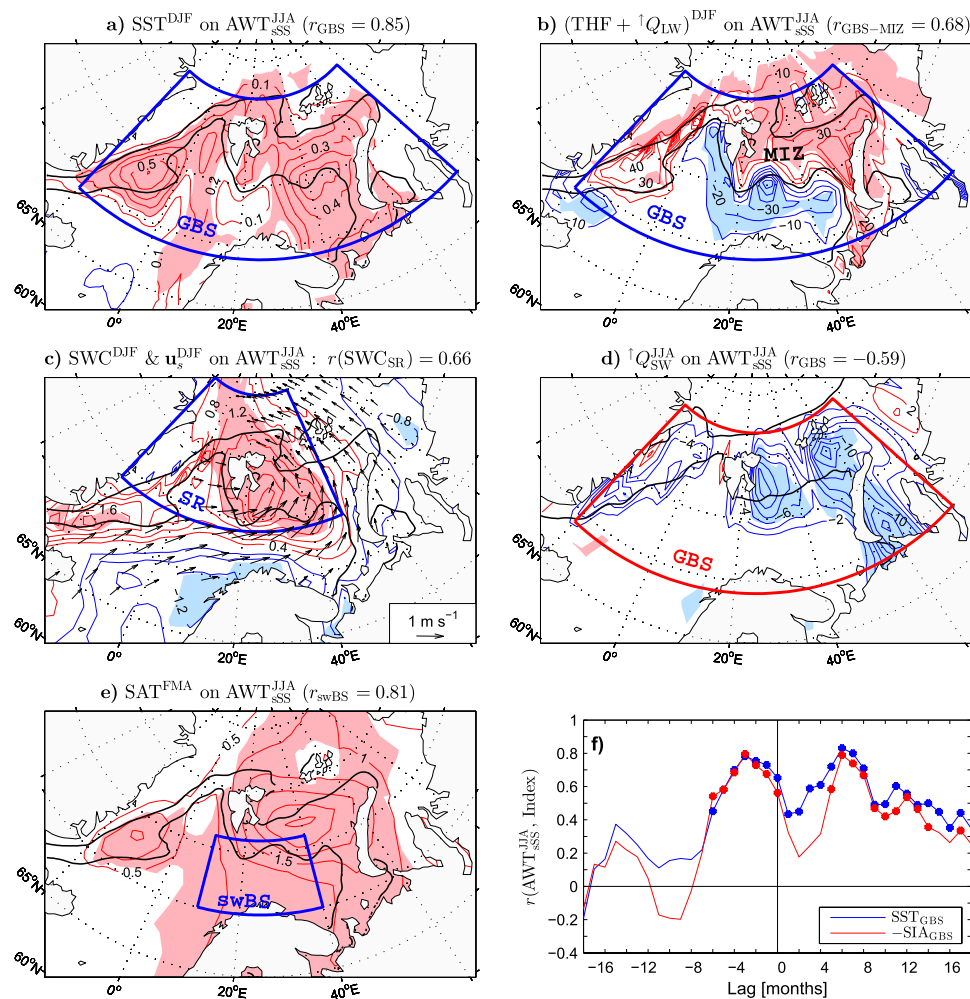
Fig. 7 a Winter SST anomalies in the Greenland–Barents Seas region (shaded if significant at $p = 0.05$, CI = 0.1 K SD^{-1}) regressed onto the preceding summer AWT_{sSS} index (blue curve in Fig. 1f). Thick black lines show the 15% and 90% contours of the climatological winter mean SIC. **b** As in **a** but for anomalies of the sum of surface turbulent (sensible + latent) heat flux and upward longwave radiation (positive upward, masked over land, CI = 10 W m^{-2} SD^{-1}). **c** As in **b** but for (thin contours) anomalies of surface wind curl (SWC, CI = 0.4×10^{-6} s^{-1} SD^{-1}). Arrows show the corresponding anomalies of surface wind velocity (subsampled and masked if both components are not significant at $p = 0.05$). **d** As in **b** but for summer anomalies of upward shortwave radiation (CI = 2 W m^{-2} SD^{-1}). **e** As in **b** but for SAT anomalies in the preceding early spring. **f** Time-lagged correlation of the summer AWT_{sSS} index with the monthly mean (blue) SST_{GBS} index (SST anomalies averaged over the GBS box in **a**) and (red) SIA_{GBS} index (sign reversed). Colour dots indicate correlations statistically significant at $p = 0.05$. The AWT_{sSS} index leads for positive lags. Lag 0 refers to the central month (July) of the summer season

increase in the MIZ and decrease on the open water side of the ice edge (Fig. 7b). In the MIZ, the more significant anomalies of ${^\uparrow}Q_{LW}$ act generally in concert with the larger THF anomalies but are counteracted by the anomalies of ${^\downarrow}Q_{LW}$ (see Table 2 for the correlations and the relative magnitude of different components of the heat flux anomalies). In open water, the anomalies of ${^\uparrow}Q_{LW}$ counteract the THF anomalies but are relatively small, as are the anomalies of ${^\downarrow}Q_{LW}$ that act in concert with the much larger THF anomalies (see the estimates for the southwestern Barents Sea in Table 2). The large downward THF anomalies along the ice edge could be driven by the

AWT_{sSS}-related cyclonic anomaly of surface winds around Svalbard (Fig. 7c), which could result from a dynamic atmospheric response to anomalous heating in the MIZ (Schlichtholz 2014). Such a response may be governed by Ekman dynamics (Schlichtholz 2013) and sustained by positive feedbacks involving wind-driven ocean circulation anomalies (Bengtsson et al. 2004), which contribute to the sea ice retreat in the Barents Sea via a coherent increase in the Atlantic water transport along the negative thermal gradient (Lien et al. 2017).

The summer AWT_{sSS} anomalies also covary significantly with the concurrent anomalies of upward shortwave

Table 2 Correlation coefficients (×100) of the summer AWT_{sSS} index of subsurface ocean temperature variability (Fig. 1f, blue curve) and the concurrent summer and the following winter SIA_{GBS} indices of sea ice variability in the Greenland–Barents Seas region with other indices of climate variability in this region for (columns r_{ESO}) the ESO period and (columns r_{ESO12}) 12 years with the strongest WACE/CAWE events (dots in Fig. 2b)

| Variable	Region	Season	Lag	Q_{ratio}	r_{ESO}			r_{ESO12}		
					AWT_{sSS}^{JJA}	SIA_{GBS}^{JJA}	SIA_{GBS}^{DJF}	AWT_{sSS}^{JJA}	SIA_{GBS}^{JJA}	SIA_{GBS}^{DJF}
SIA	GBS	DJF	6	–	–79	50	–	–89	81	–
SST	GBS	DJF	6	–	85	–50	–90	93	–82	–95
SAT	GBS-MIZ	DJF	6	–	75	–45	–95	89	–82	–98
SST	swBS	MAM	–3	–	85	–60	–64	93	–77	–84
SAT	swBS	FMA	–4	–	81	–60	–63	93	–88	–87
THF	GBS-MIZ	DJF	6	0.92	56	–ns	–62	67	–ns	–ns
$^{\uparrow}Q_{LW}$	GBS-MIZ	DJF	6	0.40	77	–46	–96	91	–84	–98
$^{\downarrow}Q_{LW}$	GBS-MIZ	DJF	6	0.36	74	–41	–93	86	–75	–97
THF	swBS	DJF	6	0.91	–67	41	74	–80	67	93
$^{\uparrow}Q_{LW}$	swBS	DJF	6	0.14	50	–ns	–77	59	–ns	–80
$^{\downarrow}Q_{LW}$	swBS	DJF	6	0.20	63	–ns	–80	68	–ns	–87
$^{\uparrow}Q_{SW}$	GBS	JJA	0	0.79	–59	90	43	–86	96	71
SIA	GBS	SON	3	–	–35	62	45	–85	94	71
SIA	GBS	JJA	0	–	–63	–	50	–91	–	81
SIA	GBS	MAM	–3	–	–83	70	56	–92	92	82

Non-significant (ns) correlations at $p = 0.05$ are not given. In column "Variable", acronyms SIA, SST, SAT, and THF refer to sea ice area, sea surface temperature, surface air temperature, and surface turbulent (sensible + latent) heat flux (positive upward), respectively. Symbols $^{\uparrow}Q_{LW}$, $^{\downarrow}Q_{LW}$, and $^{\uparrow}Q_{SW}$ denote upward longwave, downward longwave, and upward shortwave contributions to the total surface heat flux (Q_{total}). The selected indices are obtained by averaging of the specified variables over areas indicated in column "Region" (boxes marked in Fig. 7) for the season specified in column "Season" and detrended over the ESO period. Region GBS-MIZ refers to the area within the GBS box with the climatological mean SIC in the range 15–90%. Column "Lag" indicates the number of months by which the given index follows (positive value) or precedes (negative value) the AWT_{sSS}^{JJA} index. Column "Q_{ratio}" gives the ratio of the standard deviation of the anomalies of the specified heat flux component and Q_{total} for the ESO period

radiation in the MIZ. Negative anomalies of $^{\uparrow}Q_{SW}$ (corresponding to increased absorption of solar radiation and consequent warming of a thin uppermost ocean layer) are associated with warm AWT_{sSS} events (Fig. 7d). This covariability can be explained by the strong link between the summer AWT_{sSS} index and the presummer sea ice anomalies ($r = -0.83$ for the spring SIA_{GBS} index) and some persistence of the latter. Such an explanation is consistent with a high correlation of the summer SIA_{GBS} index with the concurrent $^{\uparrow}Q_{SW}$ anomalies averaged over the GBS region ($r = 0.90$) and its significant autocorrelation with the preceding spring SIA_{GBS} index ($r = 0.70$). The postsummer autocorrelation of SIA_{GBS} with its summer value decreases through autumn to winter (Table 2) and is nonsignificant when computed after regressing out the signal covariant with the summer AWT_{sSS} index (not shown). These results indicate that the effect of the ocean heat capacitor "charged" by anomalous solar heating in summer (Chung et al. 2021) on the following winter Arctic climate variability in the GBS region is less important than the effect of the ocean heat capacitor "charged" by anomalous air-sea interactions at the end of the preceding winter. However, the "solar" ocean heat capacitor may significantly contribute to winter SAT anomalies over Eurasia triggered by autumnal air-sea interactions (see Sect. 4.4).

4.1.2 Relations with the large-scale atmospheric variability

The resemblance between the winter SIC anomaly patterns associated with the concurrent WACE index (Fig. 3a) and the preceding summer AWT_{sSS} index (Fig. 1d) suggests that the atmospheric response to oceanic forcing via sea ice anomalies in the Eurasian Arctic may extend to remote regions. This inference is supported by a significant association of the strength of the polar front jet over northern Eurasia during the strong WACE/CAWE events with the summer AWT_{sSS} anomalies (Fig. 8c) and significant Eurasian lobes in the corresponding SAT and SLP anomaly patterns (Fig. 8a, b). For these events, the AWT_{sSS} anomalies explain 72% of the variance of both the WACE index and the SLP anomalies in the Ural-Siberian High region. These relationships could be anticipated from the tight coupling between the strong WACE/CAWE events and the concurrent SST and SIA anomalies in the GBS region ($r \geq 0.9$, Table 1) and from the strong linkage of the latter to the preceding summer AWT_{sSS} index ($r \approx 0.9$ for the ESO12 years; see Table 2).
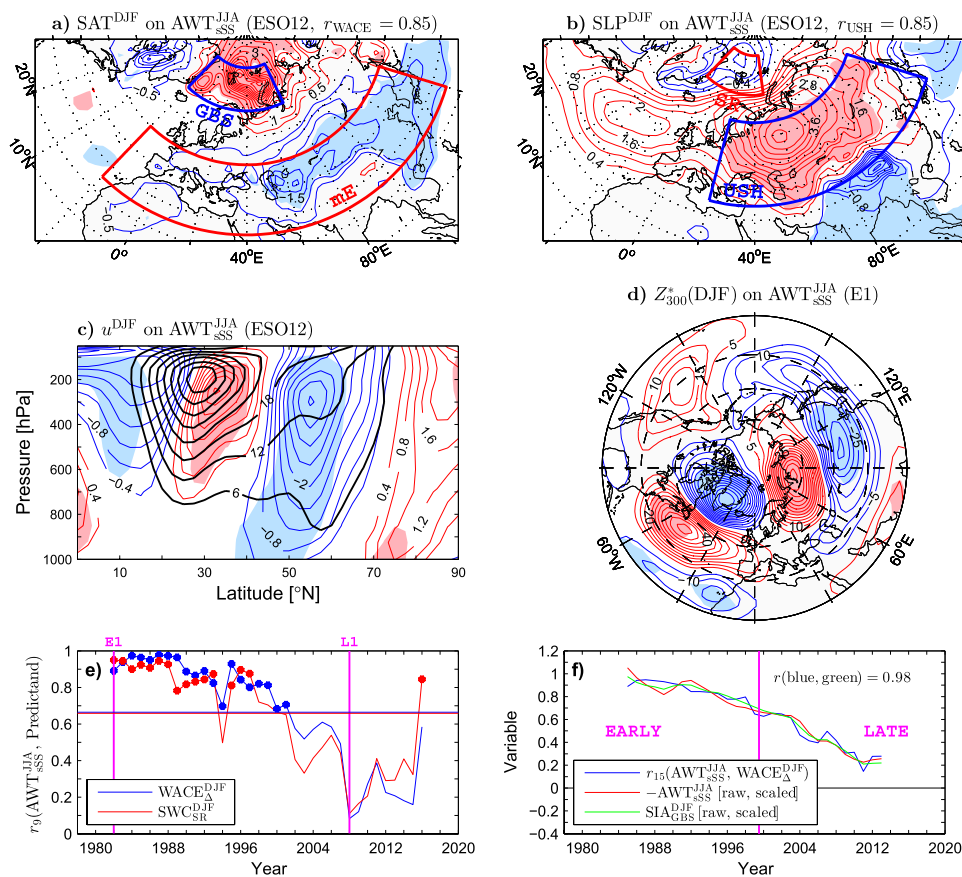
Fig. 8 a Winter SAT anomalies in the Arctic-Eurasian region (shaded if significant at $p = 0.05$, CI = 0.5 K SD^{-1}) regressed onto the preceding summer AWT$_{sSS}$ index (blue curve in Fig. 1f) for the ESO12 years (dots in Fig. 2b). **b** As in **a** but for SLP anomalies (CI = 0.4 hPa SD^{-1}). **c** As in **a** but for (thin contours) anomalies of zonal wind (u, positive eastward, averaged between 30°E and 120°E) along a latitude-vertical cross section (CI = 0.4 m s^{-1} SD^{-1}). Thick black lines show the climatological winter mean u (CI = 6 m s^{-1}). **d** As in **a** but for anomalies of the zonally asymmetric component of Z_{300} in the Northern Hemisphere extratropics (CI = 5 gpm SD^{-1}) dur-

ing the E1 subperiod (1978–1986). **e** As in Fig. 2c but for correlation of the summer AWT$_{sSS}$ index with the following winter (blue) WACE$_\Delta$ index and (red) anomalies of surface wind curl (SWC) averaged over the SR box in **b**. **f** Comparison of (blue) the 15-year moving window correlation between the summer AWT$_{sSS}$ index and the following winter WACE$_\Delta$ index with the 15-year running mean of the raw (non-detrended) scaled (non-dimensional) anomalies of (red) summer AWT$_{sSS}$ (sign reversed) and (green) winter SIA in GBS region (blue box in **a**)

One possible pathway from warm ocean temperature anomalies in the Arctic to cold air temperature anomalies over midlatitude Eurasia is through triggering regional climate feedbacks by the former. These feedbacks should contribute to the surface intensified deep warming of the Arctic troposphere associated with the diminished sea ice cover (Fig. 3f). The reduced meridional air temperature gradient across the southern rim of the anomalous Arctic warm air pool should, under the thermal wind constraint on the geostrophic flow in the hydrostatic atmosphere, weaken the vertical shear of the westerlies over northern Eurasia. This weakening should be achieved mainly via a slackening of the polar front jet, as often emphasised in the context of midlatitude linkages to Arctic amplification (Cohen et al. 2014). The slacking of the polar front jet should then lead

to more frequent or persistent high-latitude Ural blockings and, consequently, to intensification of southward cold air transport (Luo et al. 2016, 2019b). The reduced meridional temperature gradient over northern Eurasia may also contribute to the Arctic-midlatitude linkages analysed here via its effect on baroclinic instabilities generating synoptic anomalies and subsequent eddy-mean flow interactions. Such a possibility is indicated by a significant decrease in synoptic eddy activity over Eurasia in the winters following the summers with warm AWT anomalies in the Barents Sea (Schlichtholz 2016).

The WACE-AWT$_{sSS}$ linkage is also significant ($r = 0.66$) for all ESO years, but stronger in the EARLY ($r = 0.85$) than the LATE ($r = 0.46$) epoch, reflecting a recent loss of the "memory" of summer ocean temperature anomalies in the

Arctic by the winter atmosphere over Eurasia (see Table 3 for correlations of the WACE index and the SATs averaged over the Arctic and Eurasian lobes of the WACE pattern with the AWT_{sSS} index and other precursors during different periods). The changing WACE-AWT_{sSS} linkage is further illustrated by the 9-year moving window correlation between these indices (Fig. 8e, blue curve), which evolves similarly to the corresponding correlation between the AWT_{sSS} index and the anomalies of surface wind cyclonicity in the Arctic represented by the SWC_{SR} index (Fig. 8e, red curve). Both correlations take large values ($r_9 \gtrsim 0.90$) at the beginning of the EARLY epoch, including the window 1982 ± 4 (E1 in Fig. 2b) with the maximum covariability between the Arctic and Eurasian SATs (Fig. 2c). In the LATE epoch, both correlations attain a close-to-zero minimum in the window 2008 ± 4 (Fig. 8e) with all strong LATE WACE events (L1 in Fig. 2b). This minimum coincides with the LATE epoch maximum in the covariability between the Arctic and Eurasian SATs (Fig. 2c), indicating that the EARLY and LATE maxima in this covariability should have different origins. The maximum in the EARLY epoch could result from a response of quasi-stationary planetary waves to sea ice anomalies driven by persistent oceanic forcing. Such a possibility is suggested by a close relation of the winter HWI index of planetary waves variability to the concurrent SIA anomalies in the GBS region at the beginning of this epoch (Fig. 5d) and by the AWT_{sSS}-related anomaly pattern of Z_{300}^* for the E1 subperiod (Fig. 8d). An Ural blocking-like dipole accompanied by a positive NAO-like dipole in this pattern resembles the corresponding structure in the WACE-related anomaly pattern of Z_{300}^* for the entire ESO period (Fig. 5a). During E1, the HWI index correlates nearly as highly with the AWT_{sSS} anomalies ($r = 0.90$) as with the WACE index ($r = 0.96$).

The recent deterioration of the WACE-AWT_{sSS} linkage could result from changing background conditions related to the recent Arctic warming. Such a possibility is indicated by a close correspondence between the 15-year moving window correlation of the WACE index with the AWT_{sSS} anomalies and the 15-year running means of the raw (non-detrended) winter Arctic SIC anomalies in the GBS region and the summer AWT_{sSS} index itself (Fig. 8f). This finding, although somewhat uncertain due to data averaging over fixed boxes, is consistent with studies showing that the link of Eurasian climate variability to winter Arctic SIC anomalies depends on the background sea ice cover (Semenov and Latif 2015) and may be modulated on the interdecadal timescale (Sung et al. 2018), by the AMO in particular (Luo et al. 2017b; Li et al. 2018; Jin et al. 2020; Cai et al. 2023).
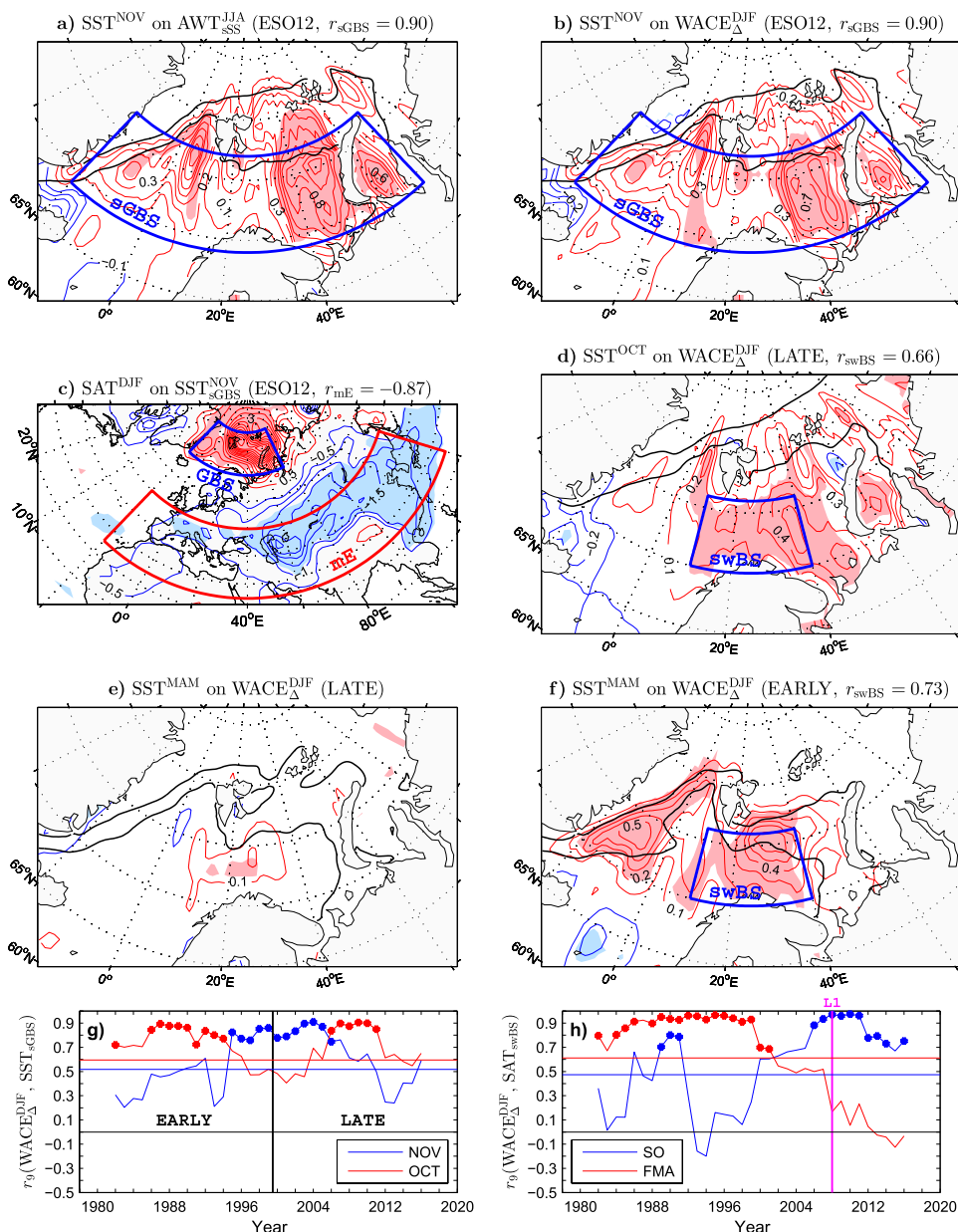
4.2 Autumn and spring sea surface temperature in the Eurasian Arctic

The above analysis reveals that the winter WACE pattern may often be triggered by sea ice anomalies in the Eurasian Arctic driven through the entrainment of earlier subsurface ocean temperature anomalies into the deepening surface mixed layer that starts at the onset of the cooling season. Therefore, significant links of autumnal SSTs in the Eurasian Arctic to both earlier ocean anomalies and later atmospheric variability can be expected. Such links are demonstrated by regressions of November (NOV) SSTs onto the preceding summer AWT_{sSS} and the following winter WACE index for the years of strong WACE/CAWE events (Fig. 9a, b, respectively). In both regressions, significant anomalies of the sign consistent with oceanic forcing of atmospheric variability (positive for the WACE events) appear in the Barents and the Greenland Sea. The winter SAT anomaly pattern in the Arctic-Eurasian region associated with the November SST_{sGBS} index of SST variability in the southern GBS region (sGBS box in Fig. 9a, b) for the ESO12 years (Fig. 9c) is similar to the AWT_{sSS}-related pattern (Fig. 8a). During these years, the summer AWT_{sSS} variability accounts for a large fraction (81%) of the variance of the November SST_{sGBS} anomalies, which on their turn explain the same fraction (81%) of the winter WACE variance.

Unlike the recent deterioration of the WACE-AWT_{sSS} linkage (Fig. 8e, f), episodes of a strong WACE relation to autumnal SSTs are found in the EARLY and LATE epochs. The timing of these episodes is different for the November and October (OCT) SSTs (compare the 9-year moving window correlations of the WACE index with the November and October SST_{sGBS} indices in Fig. 9g). For the November SSTs, continuously significant values of r_9 appear at mid-ESO windows, whereas for the October SSTs, significant values of r_9 are clustered in the mid-EARLY and mid-LATE epochs. As a result, significant values of r_9 are found for the October or November SSTs in all windows from 1986 ± 4 to 2011 ± 4.

In the LATE epoch, the most significant WACE-related October SST anomalies appear in the south-western Barents Sea (Fig. 9d). The r_9 indicator of the WACE linkage to these anomalies (averaged over the swBS box in Fig. 9d) exhibits a pronounced maximum ($r_9 = 0.98$) in the window 2008 ± 4 including all strong LATE WACE events (L1 in Fig. 2b). At that time, an equally large maximum is found in the 9-year moving window correlation between the WACE index and the preceding September-October (SO) SAT anomalies averaged over the same swBS box (Fig. 9h, blue curve). These maxima indicate that the recent WACE-related October SST anomalies in the Barents Sea could, in addition to the ocean heat transport, be influenced by a

Fig. 9 **a**, **b** November SST anomalies in the Greenland–Barents Seas region (CI = 0.1 K SD^{-1}) regressed onto the preceding summer AWT$_{sSS}$ index (blue curve in Fig. 1f) and the following winter WACE$_\Delta$ index for the ESO12 years (dots in Fig. 2b), respectively. Thick black lines show the 15% and 90% contours of the climatological mean SIC for the month of the regressed field. **c** Winter SAT anomalies in the Arctic-Eurasian region (CI = 0.5 K SD^{-1}) regressed onto the preceding November SST$_{sGBS}$ index (SST anomalies averaged over the sGBS box in **a**) for the ESO12 years. **d**, **e** As in **b** but for October and spring SST anomalies in all years of the LATE epoch (2000–2020), respectively. **f** As in **e** but for the EARLY epoch (1978–1999). **g** As in Fig. 2c but for correlation of the winter WACE$_\Delta$ index with the preceding (blue) November and (red) October SST$_{sGBS}$ index. **h** As in **g** but for correlation of the winter WACE$_\Delta$ index with the preceding (blue) September-October and (red) early spring SAT anomalies averaged over the swBS box in **d**. In **a**–**f**, anomalies significant at $p = 0.05$ are shaded

a) SST^{NOV} on AWT$_{sSS}^{JJA}$ (ESO12, $r_{sGBS} = 0.90$)

b) SST^{NOV} on WACE$_\Delta^{DJF}$ (ESO12, $r_{sGBS} = 0.90$)

c) SAT^{DJF} on SST$_{sGBS}^{NOV}$ (ESO12, $r_{mE} = -0.87$)

d) SST^{OCT} on WACE$_\Delta^{DJF}$ (LATE, $r_{swBS} = 0.66$)

e) SST^{MAM} on WACE$_\Delta^{DJF}$ (LATE)

f) SST^{MAM} on WACE$_\Delta^{DJF}$ (EARLY, $r_{swBS} = 0.73$)

quasi-simultaneous local thermodynamic atmospheric forcing. In any case, the linkage of winter WACE variability to the preceding spring SSTs in the Eurasian Arctic is negligible during the LATE epoch (Fig. 9e). By contrast, the corresponding association is considerable in the EARLY epoch when significant WACE-related spring SST anomalies appear in the Greenland and the Barents Sea (Fig. 9f). These anomalies should also result from a quasi-simultaneous local atmospheric forcing, as indicated in Fig. 9h (red curve) by the 9-year moving window correlation of the winter WACE index with the preceding early spring SATs averaged over the south-western Barents Sea (swBS box in Fig. 9f). Similarly to the WACE-AWT$_{sSS}$ linkage (Fig. 8e), this correlation remains significant throughout the EARLY

epoch and then deteriorates. This is not surprising given that the summer subsurface ocean temperature anomalies in the Barents Sea strongly depend on local air-sea interactions during the previous winter-to-spring season (see Sect. 4.1.1). Since these anomalies are also significantly associated with the following winter SSTs in the North Atlantic (Schlichtholz 2016), below we will check if and when the winter WACE variability is related to reemerging SST anomalies in this ocean.

Fig. 10 **a**–**c** SST anomalies in the Arctic-North Atlantic region (CI = 0.1 K SD^{-1}) in early spring, summer, and autumn, respectively, regressed onto the following winter WACE$_\Delta$ index (blue curve in Fig. 2b) for the EARLY epoch (1978–1999). Thick black lines show the 15% and 90% contours of the mean SIC for the season of the regressed field. **d** As in **a**–**c** but for winter (lag 0) SST anomalies. **e** As in **c** but for autumn SST anomalies in the LATE epoch (2000–2020). **f** As in Fig. 2c but for correlation of the winter WACE$_\Delta$ index with (red) the preceding autumn ΔSST_{NA} index (difference between standardised SST anomalies averaged over the GSE and nwNA boxes in **c**) and (blue) the preceding early spring SST anomalies averaged over the swBS box in **a**. In **a**–**e**, anomalies significant at $p = 0.05$ are shaded
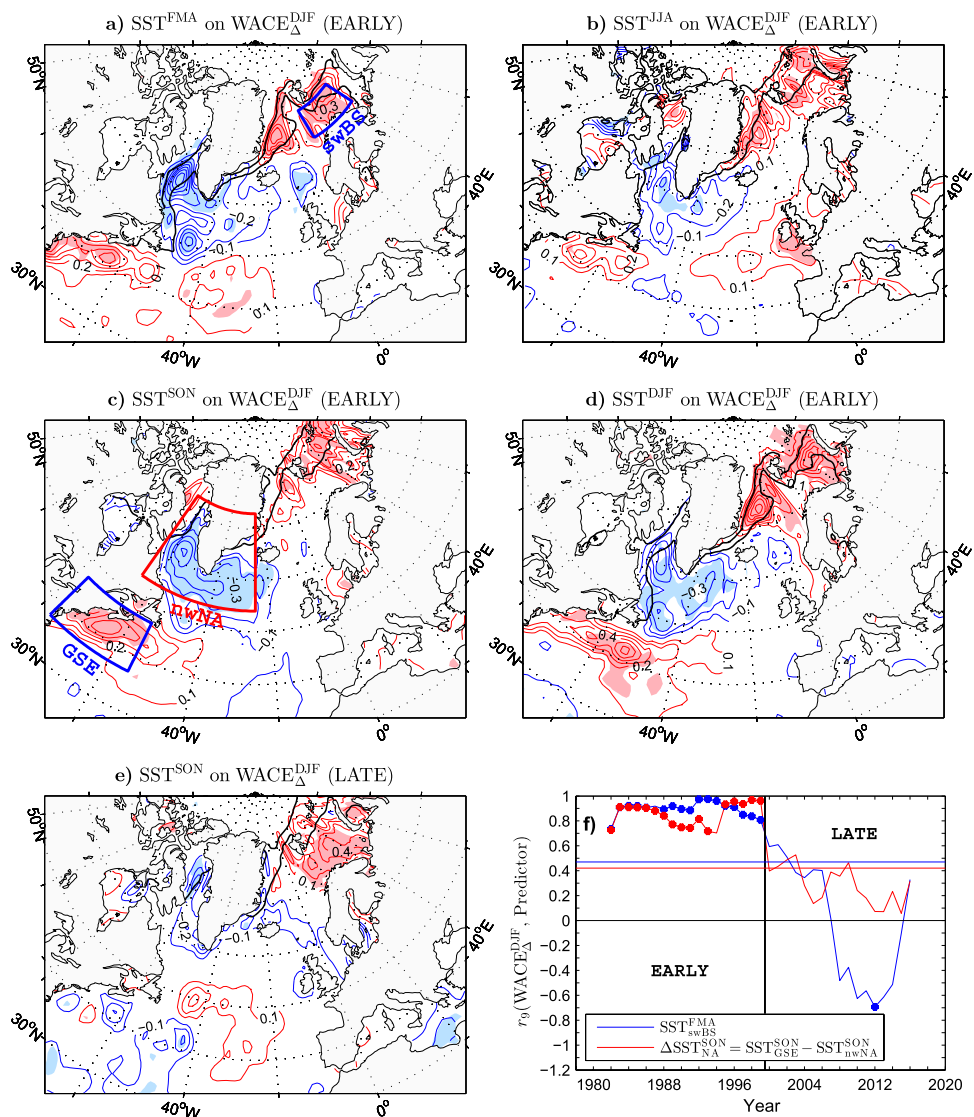
4.3 Spring-to-autumn sea surface temperature in the North Atlantic

As shown above, the winter WACE variability is related to earlier ocean temperature anomalies in the Eurasian Arctic (Figs. 8, 9). Since this variability is also related to concurrent SST anomalies in the North Atlantic (Sato et al. 2014; Li et al. 2021), it is of interest to check whether and when it may represent a mode of Arctic-midlatitude linkages influenced by a large-scale pattern of earlier SST anomalies. The working hypothesis is that such a mode is somehow related to reemerging SST anomalies in the Arctic-North Atlantic sector. To test this hypothesis, Fig. 10a–d shows the SST anomaly pattern in this sector associated with the winter WACE index during the EARLY epoch for the preceding early spring, summer, and autumn and for the concurrent winter. The early spring pattern exhibits significant warming not only in the Barents and Greenland Seas but also

in the Gulf Stream extension area and significant cooling in the north-western North Atlantic region, including the Labrador Sea (Fig. 10a). This pattern weakens in summer (Fig. 10b) when the subsurface remnants of heat anomalies accumulated at the end of winter in the deep surface mixed layer are shielded from thermodynamic air-sea interactions by a shallow seasonal pycnocline. Consistent with the SST reemergence mechanism (Deser et al. 2003), the pattern is then reinforced in autumn (Fig. 10c) due to the entrainment of persistent subsurface heat anomalies into the deepening surface mixed layer. The pattern persists until winter, when it even strengthens in the Eurasian Arctic (Fig. 10d), probably due to further deepening of the surface mixed layer and atmosphere-ice-ocean feedbacks.

In contrast to the EARLY epoch, in the LATE epoch, the winter WACE variability is still significantly linked to the preceding autumn SST anomalies in the Barents Sea but not in the North Atlantic (Fig. 10e). Therefore, it is

Table 3 Correlation coefficient r ($\times 100$) of the winter $WACE_\Delta$, SAT_{GBS}, and SAT_{mE} indices (defined in Table 1) with selected predictors for the 12 strongest WACE/CAWE events (dots in Fig. 2b) during the ESO period (column r_{ESO12}) and for the year-to-year anomalies during its EARLY (column r_{EARLY}) and LATE (column r_{LATE}) epochs

Symbol	Region	Domain/Method	Season	r_{ESO12}	r_{EARLY}	r_{LATE}
AWT_{sSS}	Southern Svalbard slope	73°–75°N, 13°–20°E	JJA	85 (84, – 79)	85 (75, – 77)	46 (68, – ns)
SST_{sGBS}	Southern Greenland–Barents Seas	69°–77°N, 20°W–70°E	NOV	90 (86, – 87)	50 (48, – ns)	51 (63, – ns)
SST_{sGBS}			OCT	88 (87, – 83)	69 (55, – 70)	53 (65, – ns)
SST_{swBS}	South-western Barents Sea	70°–76°N, 10°–40°E	NOV	69 (64, – 68)	ns (ns, ns)	63 (72, – ns)
SST_{swBS}			OCT	81 (80, – 76)	48 (62, – ns)	64 (72, – ns)
SST_{swBS}			MAM	77 (83, – 65)	73 (66, – 65)	ns (48, – ns)
SST_{GLS}	Greenland-to-Laptiev Seas	69°–83°N, 20°W–145°E	OCT	84 (82, – 79)	61 (ns, – 68)	53 (56, – ns)
SIA_{GLS}			SON	– 71 (– 65, 70)	– 53 (– ns, 65)	– ns (– ns, ns)
SIA_{GLS}			JJA	– 81 (– 79, 76)	– 61 (– ns, 79)	– ns (– ns, ns)
SIA_{GLS}			MAM	– 81 (– 77, 78)	– 71 (– 52, 78)	– ns (– ns, ns)
$(^\uparrow Q_{SW})_{GLS}$			JJA	– 73 (– 72, 67)	– 70 (– 44, 84)	– ns (– ns, ns)
THF_{BS-MIZ}	Barents Sea MIZ	69°–82°N, 15°–75°E	NOV	87 (81, – 86)	48 (43, – 43)	63 (51, – 57)
THF_{sBS}	Southern Barents Sea	67°–76°N, 15°–75°E	NOV	65 (64, – 60)	40 (ns, – 40)	45 (ns, – ns)
THF_{sBS}			OCT	– ns (– ns, ns)	ns (ns, – ns)	– ns (– ns, ns)
THF_{nGLS}	Northern Greenland-to-Laptiev Seas	78°–82°N, 10°W–145°E	OCT	ns (ns, – 59)	ns (ns, – 44)	48 (ns, – 45)
SST_{GSE}	Gulf Stream extension	37°–47°N, 80°–55°W	SON	ns (ns, – ns)	68 (74, – 51)	– ns (ns, ns)
SST_{nwNA}	North-western North Atlantic	54°–73°N, 65°–25°W	SON	– 63 (– 61, 59)	– 59 (– 58, 55)	– ns (– ns, ns)
ΔSST_{NA}	North Atlantic	$SST_{GSE} - SST_{nwNA}$	SON	59 (64, – ns)	76 (75, – 61)	ns (ns, ns)
ΔSST_{NA}			OCT	72 (75, – 63)	76 (71, – 64)	ns (ns, – ns)
SST_{cNP}	Central North Pacific	30°–42°N, 175°–158°W	NOV	77 (82, – 66)	ns (ns, – ns)	70 (73, – 49)
SST_{neNP}	North-eastern North Pacific	magenta box in Fig. 15a	NOV	– 75 (– 66, 77)	– ns (– ns, ns)	– 53 (– 45, 46)
SST_{seNP}	South-eastern North Pacific	10°–20°N, 160°–115°W	NOV	– 58 (– ns, 59)	– ns (– ns, ns)	– 59 (– ns, 77)
ΔSST_{nNP}	Northern North Pacific	$SST_{cNP} - SST_{neNP}$	NOV	80 (79, – 75)	ns (42, – ns)	72 (68, – 55)
ΔSST_{sNP}	Southern North Pacific	$SST_{cNP} - SST_{seNP}$	NOV	73 (73, – 67)	ns (ns, – ns)	81 (57, – 78)
PDO	North Pacific	Mantua et al. (1997)	NOV	– ns (– ns, ns)	– ns (– ns, ns)	– 53 (– ns, 48)
NINO3	Equatorial Pacific	5°S-5°N, 150°–90°W	NOV	– ns (– ns, ns)	– ns (– ns, ns)	– ns (– ns, 48)
AMO	North Atlantic	North of 0°N	SON	– ns (– ns, ns)	– ns (– ns, ns)	– ns (– ns, ns)

The correlations for SAT_{GBS} and SAT_{mE} are given in parenthesis (from left to right, respectively) after the correlation for $WACE_\Delta$. The correlations for the ESO12 years are computed from data detrended over the ESO period (1978–2020, years of December), whereas the correlations for the EARLY (1978–1999) and LATE (2000–2020) epochs are based on data detrended over these epochs. Non-significant (ns) correlations at $p = 0.05$ are not given. Except for the Pacific Decadal Oscillation (PDO) index, the selected predictors are obtained by averaging over the area given in column "Domain/Method" or by subtracting the standardised values of the indices indicated in that column. Column "Season" indicates the season/month of the predictor. In column "Symbol", acronyms AWT, SST, SIA, and THF stand for Atlantic water temperature, sea surface temperature, sea ice area, and surface turbulent (sensible + latent) heat flux (positive upward), respectively. Symbol $^\uparrow Q_{SW}$ denotes surface upward shortwave radiation flux. Acronyms in the subscript denote regions indicated in column "Region". Acronym MIZ refers to the area with the climatological mean SIC in the range 15–90%. Acronyms NINO3 and AMO refer to SST indices of El Niño and Atlantic Multidecadal Oscillation, respectively

unlikely that the recent WACE variability is driven by the reemerging SST anomalies in the North Atlantic or the Eurasian Arctic where, in the LATE epoch, the springtime SSTs are not significantly related to the following winter WACE index (Fig. 9e). The recent deterioration of the winter WACE relation to the reemerging SST anomalies in the Arctic-North Atlantic sector is further illustrated in Fig. 10f, which shows the 9-year moving window correlation of the WACE index with the preceding early spring SST_{swBS} index of SST variability in the south-western Barents Sea (swBS box in Fig. 10a) and the preceding autumn ΔSST_{NA} index of SST variability in the North Atlantic. The latter is defined as the difference ($SST_{GSE} - SST_{nwNA}$) between SSTs averaged over the Gulf Stream extension area and the north-western North Atlantic region (GSE and nwNA boxes in Fig. 10c, respectively). For both SST indices, their correlation with the WACE index remains significant from the beginning of the time series until the window 1999 ± 4 including several strong CAWE events (EL in Fig. 2b) and then drops to insignificant values (Fig. 10f). A similar drop is found for the North Atlantic dipolar SST anomaly in the month (October) in which this

anomaly is most significantly related to the following winter WACE variability during the ESO period (not shown, but see the correlations in Table 3).

The moving window correlations in Fig. 10f evolve consistently with the corresponding correlations of the WACE index with the non-SST indices of Arctic climate variability related to reemerging SST anomalies, such as the anomalies of early spring air temperature (forcing factor) and summer subsurface ocean temperature (seasonal memory factor) in the Barents Sea region (Figs. 9h, 8e). Collectively, these lagged correlations indicate that the Barents Sea is not merely an amplifier of the remote atmospheric response to wintertime oceanic forcing over the Gulf Stream region through the sea ice anomalies induced by this response, as suggested in some studies (Sato et al. 2014; Simmonds and Govekar 2014; Jung et al. 2017). These correlations and the significant recent WACE link to

autumnal SST anomalies in the Barents Sea (Figs. 10e, 9d) driven by a quasi-simultaneous rather than earlier local atmospheric forcing (Fig. 9h) suggest that the atmospheric response to oceanic anomalies in the Eurasian Arctic, regardless of their origin and teleconnections, is a key factor shaping the winter WACE variability throughout the ESO period. Before discussing the teleconnections in the LATE epoch, below we will analyse the WACE linkage to surface conditions in the Arctic from the perspective of earlier sea ice anomalies and air-sea heat exchanges.

4.4 Spring-to-autumn sea ice concentration in the Barents Sea and adjacent areas

As the winter WACE pattern may "remember" not only earlier ocean temperature anomalies in the Eurasian Arctic
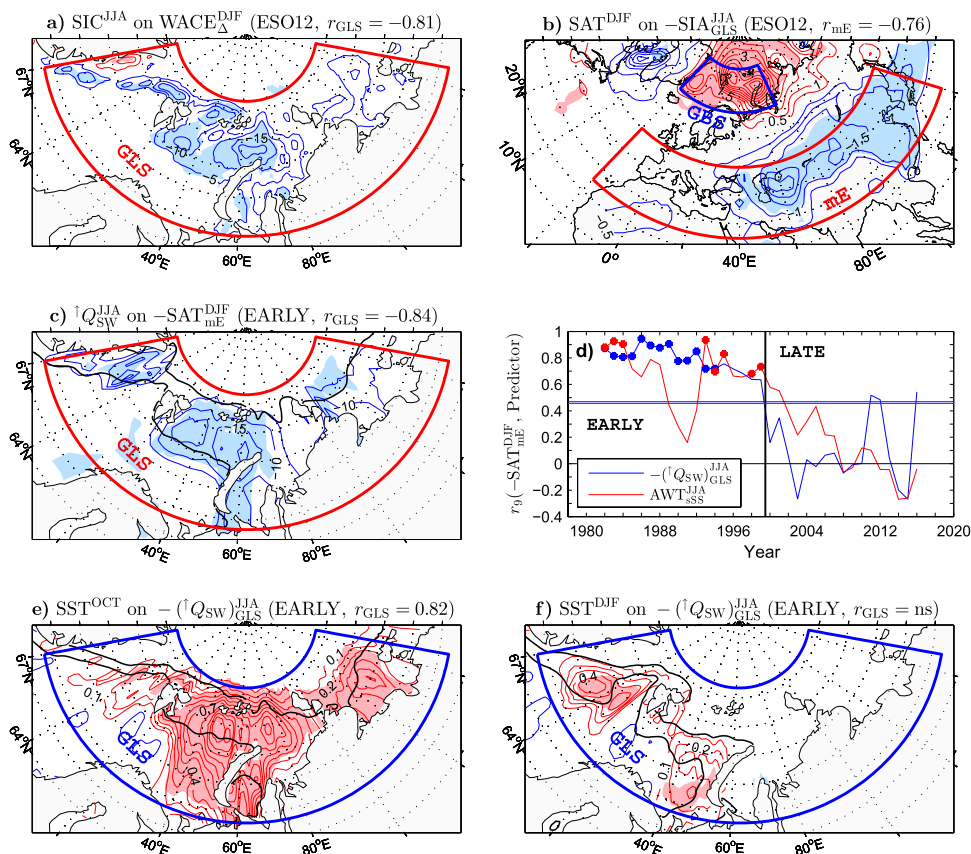
Fig. 11 a Summer SIC anomalies in the Greenland-to-Laptiev Seas region (CI = 5% SD^{-1}) regressed onto the following winter WACE$_\Delta$ index for the ESO12 years (dots in Fig. 2b). **b** Winter SAT anomalies in the Arctic-Eurasian region (CI = 0.5 K SD^{-1}) regressed onto the preceding summer SIA anomalies (sign reversed) averaged over the GLS box in **a** for the ESO12 years. **c** As in **a** but for (thin contours) summer anomalies of upward shortwave radiation ($^\uparrow Q_{SW}$, CI = 5 W m^{-2} SD^{-1}) regressed onto the following winter SAT$_{mE}$ index (sign reversed) of SAT variability over midlatitude Eurasia (mE box in **b**) for all years in the EARLY epoch (1978–1999). Thick black

lines show the 15% and 90% contours of the mean SIC for the season of the regressed field. **d** As in Fig. 2c but for correlation of the winter SAT$_{mE}$ index (sign reversed) with (blue) the preceding summer ($^\uparrow Q_{SW}$)$_{GLS}$ index ($^\uparrow Q_{SW}$ averaged over the GLS box in **c**, sign reversed) and (red) the preceding summer AWT$_{sSS}$ index (blue curve in Fig. 1f). **e, f** As in **c** but for SST anomalies in October and winter (CI = 0.1 K SD^{-1}) regressed onto the preceding summer ($^\uparrow Q_{SW}$)$_{GLS}$ index (sign reversed), respectively. In **a–c**, **e**, and **f**, anomalies significant at $p = 0.05$ are shaded

(Figs. 8, 9) and the North Atlantic (Fig. 10) but also earlier Arctic sea ice anomalies (Jang et al. 2021; Zhang and Screen 2021), it is interesting to compare lagged WACE linkages to sea ice and ocean temperature variability. We find that the strong winter WACE/CAWE events in the ESO period are significantly related to seasonal mean sea ice cover anomalies in the Barents and adjacent Arctic marginal seas during the preceding autumn, summer, and spring, with the WACE events corresponding to a low sea ice cover. As an example, Fig. 11a shows the summer SIC anomaly pattern associated with the strong winter WACE/CAWE events, and Fig. 11b shows the SAT anomaly pattern during these events associated with the summer SIA_{GLS} index of SIC anomalies (sign reversed) integrated over the area extending from the Greenland Sea to the Laptiev Sea (GLS box in Fig. 11a). The latter pattern resembles the corresponding pattern associated with the summer AWT_{sSS} index of ocean temperature variability in the Barents Sea (Fig. 8a). The summer SIA_{GLS} anomalies account for almost the same fraction (66%) of the variance of the strong WACE/CAWE events in the following winter as the summer AWT_{sSS} anomalies do. The corresponding

linkage is slightly weaker for the autumn SICs but equally strong for the SIC anomalies in spring (Table 3), which should be a side effect of a common forcing of the latter and persistent ocean temperature anomalies that influence the following winter sea ice and atmospheric variability (see Sect. 4.1.1).

While the year-to-year linkage of winter WACE variability to the preceding spring-to-autumn SIA_{GLS} anomalies is significant in the EARLY epoch, it is not in the LATE epoch (Table 3). In the EARLY epoch, the spring-to-autumn SIA_{GLS} anomalies are associated by far more significantly with the following winter SAT anomalies over the Eurasian lobe (mE box in Fig. 11b) than the Arctic lobe (GBS box in Fig. 11b) of the typical WACE pattern (Table 3). These relationships suggest that the mechanism of the "solar" ocean heat capacitor related to summertime changes in Arctic sea ice cover (Chung et al. 2021) can sometimes drive winter SAT anomalies in Eurasia. Consistent with this scenario, in the EARLY epoch, the summer anomaly pattern of $^\uparrow Q_{SW}$ in the Arctic associated with the following winter SAT_{mE} index (shown in Fig. 11c with sign reversed)

Fig. 12 **a–c** November anomalies of geopotential height at 50 hPa (Z_{50}) in the Northern Hemisphere extratropics (CI = 10 gpm SD^{-1}) regressed onto the preceding summer anomalies of $^\uparrow Q_{SW}$ (sign reversed) averaged over the GLS box in Fig 11c, summer AWT_{sSS} index (blue curve in Fig. 1f), and October THF anomalies averaged over the sBS box in Fig 13c during the E1 subperiod (1978–1986), respectively. **d** As in **c** but for November anomalies of Z_{50} regressed onto the preceding October THF anomalies averaged over the nGLS box in Fig 13e during the L1 (2004–2012) subperiod. In **a–d**, anomalies significant at $p = 0.05$ are shaded. Black contours show the mean field of Z_{50} over the given subperiod (CI = 0.2×10^3 gpm)
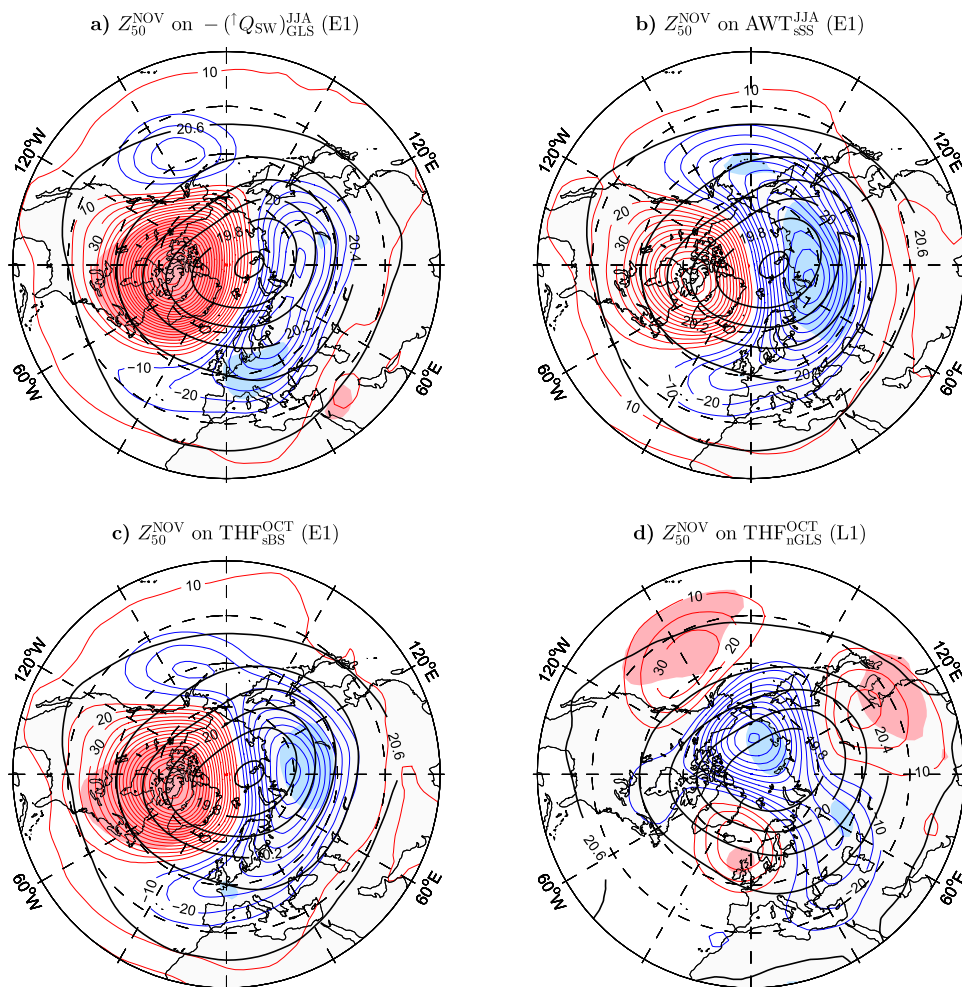
exhibits significant anomalies in the Laptiev Sea as well as the GBS area. The summer anomalies of $^\uparrow Q_{SW}$ averaged over the entire GLS region correlate positively with and explain a large fraction ($r = 0.84$) of the following winter SAT_{mE} anomalies, indicating that cold winters in Eurasia are favoured by excessive summertime ocean heat storage in the Arctic due to decrease in upward shortwave radiation at the surface instigated by lowered SICs. The release of this heat to the atmosphere should occur in autumn, as implied by a strong linkage of October SSTs and a weak linkage of winter SSTs to the preceding summer anomalies of $^\uparrow Q_{SW}$ in the GLS region (see Fig. 11e, f for the regression patterns).

The remote atmospheric response to the heat release by the "solar" ocean heat capacitor could involve a stratospheric pathway, especially at the beginning of the EARLY epoch when all strong EARLY WACE events occurred (Fig. 2b). This possibility is supported by the anomaly pattern of geopotential height at 50 hPa (Z_{50}) in November associated with the preceding summer anomalies of $^\uparrow Q_{SW}$ in the GLS region for the E1 subperiod (see Fig. 12a for the anomalies with sign reversed and the mean field of Z_{50} in November). According to this pattern, increased solar heating of the ocean is followed by a shift of the stratospheric polar vortex towards Eurasia. In general terms, this result is in line with studies showing linkages of Eurasian cold events in winter to late autumn Arctic sea ice loss via intensification of the Ural blocking pattern by a downward influence of the stratospheric circulation anomaly excited by changes in the propagation of planetary waves from the troposphere into the stratosphere (Kim et al. 2014; Zhang et al. 2018). However, these studies emphasise the tropospheric response to a weakening of the polar vortex in winter rather than its shifting in autumn.

Continuously significant values of the 9-year moving window correlation between the summer anomalies of $^\uparrow Q_{SW}$ in the GLS region and the following winter SAT_{mE} index persist through the EARLY epoch until the window 1994 ± 4 (Fig. 11d, blue curve). The corresponding association of the Eurasian SATs with the preceding summer AWT_{sSS} anomalies exhibits a considerable temporary weakening around the window 1991 ± 4 (Fig. 11d, red curve) without any strong WACE/CAWE event (E2 in Fig. 2b). This weakening and the equally strong overall linkage of the Eurasian and Arctic SATs to the AWT_{sSS} variability in the EARLY epoch (Table 3) indicate that, in that epoch, the delayed atmospheric response to ocean thermal anomalies driven by air-sea interactions in the winter-to-spring season rather than through changes in summertime solar heat absorption is critical for the following winter WACE variability. While the reemerging Arctic SST anomalies influence atmospheric variability mainly through their effect on the winter sea ice extent (see Sect. 4.1.1), they may also modify the stratospheric pathway, as suggested by the AWT

$_{sSS}$-related pattern of November anomalies of Z_{50} for the E1 subperiod (Fig. 12b). This pattern resembles the corresponding pattern associated with the summer anomalies of $^\uparrow Q_{SW}$ in the GLS region (Fig. 12a) but exhibits a more significant lobe over northern Eurasia. In the following, we will show that the strong WACE events are closely related to autumnal air-sea heat exchanges in the Eurasian Arctic during both the EARLY and the LATE epoch.

4.5 Autumn air-sea heat exchanges in the Barents Sea and adjacent areas

Sorokina et al. (2016) found that anomalous turbulent heat fluxes in the Eurasian Arctic during the months preceding winter WACE events are insignificant or appear in open water rather than in the area of sea ice decline and concluded that causal links between autumnal surface conditions in the Arctic and winter WACE variability are doubtful. However, the forcing of atmospheric variability by increased open water THFs is consistent with significant relations of the WACE pattern to earlier ocean temperature anomalies in the Barents Sea demonstrated in previous sections (Figs. 8, 9). Moreover, the WACE index used by these authors was based on data from a domain limited in the south to the 45°N parallel, while most of the significant WACE-related Eurasian SAT anomalies appear south of this parallel (Fig. 2a). The winter WACE index used in the present study is significantly related to November THF anomalies in the Barents Sea region, with the WACE events generally following enhanced ocean heat loss to the atmosphere in the MIZ as well as over open water (Fig. 13a). Figure 13b shows the winter SAT anomaly pattern associated with the preceding November THF_{BS-MIZ} index of air-sea heat exchange variability in the Barents Sea MIZ (based on THFs integrated between the black contours within the BS box in Fig. 13a) for the strong WACE/CAWE events. This pattern is similar to the pattern associated with the previous summer AWT_{sSS} index of ocean temperature variability (Fig. 8a). In both patterns, significant warming in the Eurasian Arctic is accompanied by significant cooling in the area between the Caspian Sea and the Pacific coast of Asia, indicating that ocean thermal anomalies in the Arctic influence remote atmospheric variability through their impact on not only wintertime but also autumnal air-sea heat exchanges. Consistent with this scenario, the November THF_{BS-MIZ} index explains about the same fraction (76%) of the variance of the strong WACE/CAWE events as the summer AWT_{sSS} index and autumnal SSTs in the Eurasian Arctic do (Table 3).

A remarkable feature of winter WACE variability is its strong linkage to the preceding October air-sea heat exchanges in the Arctic during the EARLY and the LATE epoch maximum covariability between the SAT anomalies
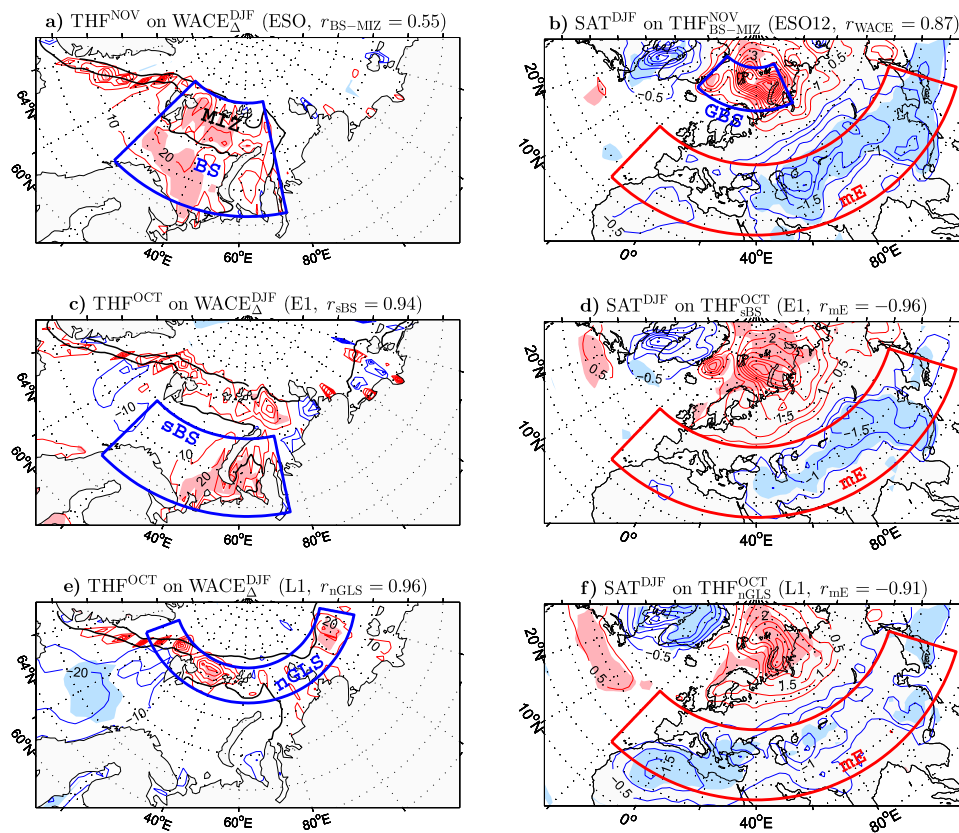
Fig. 13 a November THF anomalies (positive upward, masked over land) in the Greenland-to-Laptiev Seas region (CI = 10 W m^{-2} SD^{-1}) regressed onto the following winter WACE$_\Delta$ index (blue curve in Fig. 2b). Thick black lines show the 15% and 90% contours of the mean SIC for the month of the regressed field. **b** Winter SAT anomalies in the Arctic-Eurasian region (CI = 0.5 K SD^{-1}) regressed onto the preceding November THF anomalies averaged over the Barents Sea marginal ice zone (between the black contours within the BS box in **a**) for the ESO12 years (dots in Fig. 2b). **c, e** As in **a** but for October THF anomalies during the E1 (1978–1986) and L1 (2004–2012) subperiods, respectively. **d, f** As in **b** but for winter SAT anomalies regressed onto the preceding October THF anomalies averaged over the sBS box in **c** and the nGLS box in **e** during the E1 and L1 subperiods, respectively. In **a–f**, anomalies significant at $p = 0.05$ are shaded
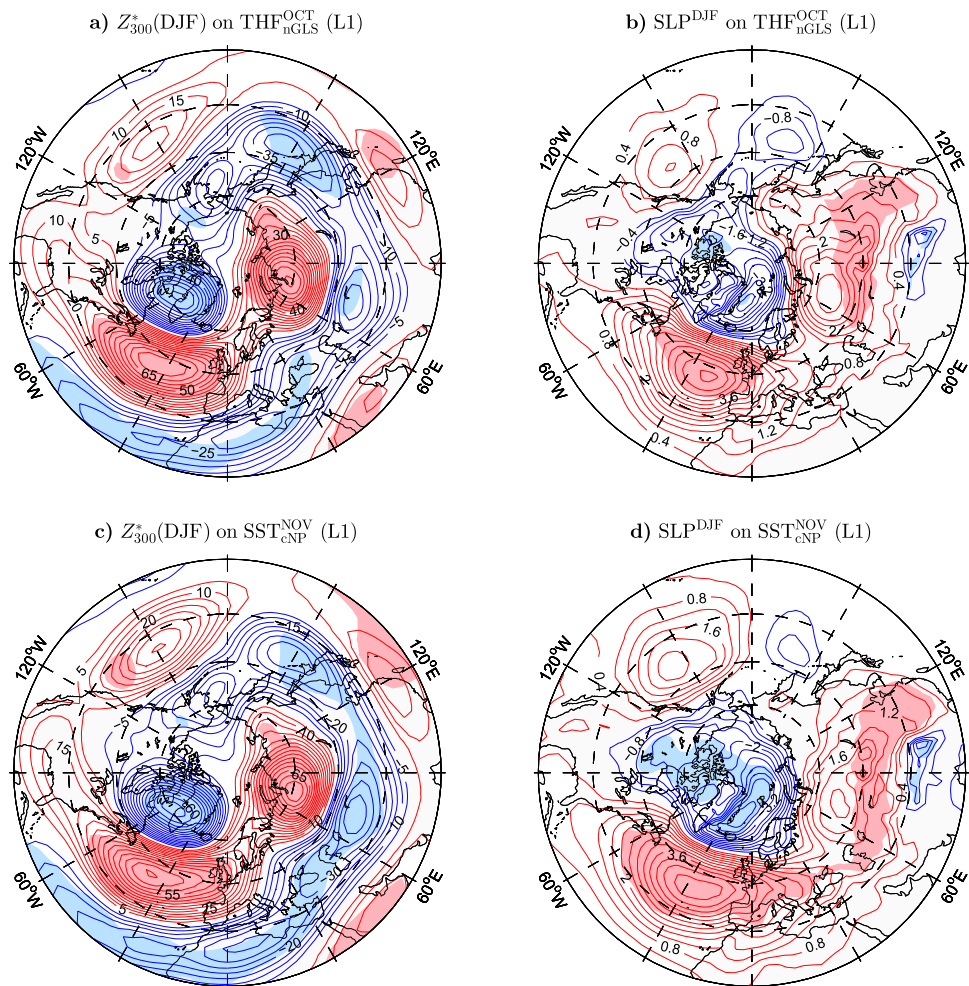
averaged over the Arctic and the Eurasian lobe of the typical WACE pattern (GBS and mE boxes in Fig. 13b), namely during the E1 and L1 subperiods (see Fig. 2b, c). However, the WACE-related pattern of October THF anomalies is different in these subperiods. In E1, the winter WACE events follow enhanced Ocober THFs over both the northern and the southern Barents Sea but more significantly in the south (Fig. 13c). In this subperiod, the variability of the October THF$_{sBS}$ index (computed from THFs averaged over the sBS box in Fig. 13c) represents mainly anomalous air-sea heat exchanges driven by the ocean, as indicated by its high correlation with the preceding summer AWT$_{sSS}$ index ($r = 0.88$) and upward shortwave radiation anomalies integrated over the sBS area ($r = -0.84$). In L1, the winter WACE events are associated with October THFs that are significantly enhanced in the MIZ on the northern rim of the Laptiev Sea and along the continental slope of the northern Barents Sea but significantly reduced in open water (Fig. 13e). This dipolar pattern of THF anomalies reflects a quasi-simultaneous

atmospheric forcing of sea ice and ocean temperature anomalies, as indicated by the already noted association of the winter WACE variability with autumnal SSTs and SATs in the Barents Sea area, which is most significant just around the L1 subperiod (Fig. 9d, h). In this subperiod, the October THF$_{nGLS}$ index of air-sea heat exchange variability in the MIZ (computed from THFs averaged over the nGLS box in Fig. 13e) accounts for about the same fraction of the variance of the following winter WACE variability (92%) and SAT anomalies over the Eurasian lobe of the WACE pattern (83%) as the THF$_{sBS}$ index does in E1.

In the Arctic-Eurasian sector, compared to the THF$_{sBS}$-related SAT anomaly pattern in E1 (Fig. 13d), the THF$_{nGLS}$-related SAT anomaly pattern in L1 (Fig. 13f) exhibits significant Arctic anomalies over the Barents-Kara rather than the Greenland–Barents Seas. In the mid-latitudes, it exhibits significant anomalies not only in Asia but also in the Mediterranean region. The differences in the Arctic probably reflect nuances of local atmosphere-ice-ocean feedbacks

Fig. 14 **a** Winter anomalies of the zonally asymmetric component of Z_{300} in the Northern Hemisphere extratropics (CI = 5 gpm SD^{-1}) regressed onto the preceding October THF anomalies averaged over the northern Greenland-to-Laptiev Seas region (nGLS box in Fig. 13e) during the L1 (2004–2012) subperiod. **b** As in **a** but for SLP anomalies (CI = 0.4 hPa SD^{-1}). **c, d** As in **a, b** but for winter anomalies of Z_{300}^* and SLP regressed onto the preceding November SST anomalies averaged over the central North Pacific (cNP box in Fig. 15a). In **a–d**, anomalies significant at $p = 0.05$ are shaded

a) Z_{300}^*(DJF) on THF$_{nGLS}^{OCT}$ (L1)

b) SLP^{DJF} on THF$_{nGLS}^{OCT}$ (L1)

c) Z_{300}^*(DJF) on SST$_{cNP}^{NOV}$ (L1)

d) SLP^{DJF} on SST$_{cNP}^{NOV}$ (L1)

under different background conditions during E1 and L1. The differences in the mid-latitudes are related to the anatomy of upper-level distortions of the quasi-stationary planetary waves. In E1, the THF$_{sBS}$-related anomaly pattern of Z_{300}^* (not shown) mirrors the corresponding AWT$_{sSS}$-related pattern (Fig. 8d). In both patterns, the NAO-like dipole in the Arctic-North Atlantic sector tilts northeastward, and its Arctic trough is centred over southern Greenland. In the corresponding THF$_{nGLS}$-related pattern for L1, the NAO-like dipole tilts northwestward (Fig. 14a). Its Arctic trough is centred over Baffin Bay, whereas its North Atlantic ridge is more significant and displaced towards Europe. As a result, the surface counterpart of the upper-level ridge is also strong and centred closer to Europe in L1 (see Fig. 14b for the THF$_{nGLS}$-related SLP anomaly pattern). Cold-air advection on its south-eastern rim can explain the cooling in the Mediterranean region (Fig. 13f). Similarly, differences in the location of the most significant Asian SAT anomalies between E1 and L1 (Fig. 13d, f) can be attributed to differences in

the Asian upper-level trough of the anomalous midlatitude planetary wave. During L1, this trough is split into a core located east of the Caspian Sea and a core centred over the western North Pacific (Fig. 14a). These differences might be related to a different stratospheric pathway of the signal, as suggested by comparison of November anomaly patterns of Z_{50} associated with the October anomalies of THF$_{sBS}$ in E1 and THF$_{nGLS}$ in L1 (Fig. 12c, d). The THF$_{sBS}$-related pattern, which shows a shift of the polar vortex towards Eurasia (Fig. 12c), is consistent with the corresponding patterns associated with the summer anomalies of $^\uparrow Q_{SW}$ and AWT in the Eurasian Arctic (Fig. 12a, b). The THF$_{nGLS}$-related pattern exhibits a strengthening of the polar vortex instead (Fig. 12d).

4.6 Autumn sea surface temperature in the North Pacific

Unlike the relation of winter WACE variability to autumn SST anomalies in the North Atlantic, significant in the EARLY but not the LATE epoch (Fig. 10c, e), its relation to
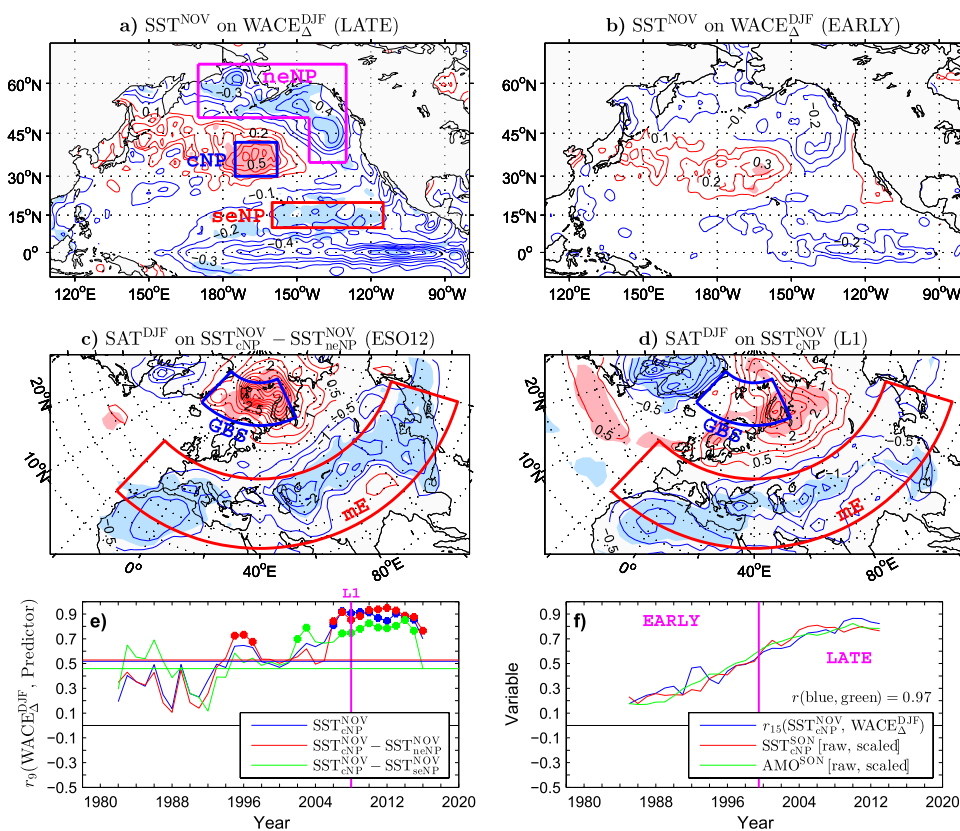
Fig. 15 **a**, **b** November SST anomalies in the North Pacific (CI = 0.1 K SD^{-1}) regressed onto the following winter WACE$_\Delta$ index (blue curve in Fig. 2b) for the LATE (2000–2020) and the EARLY (1978–1999) epoch, respectively. **c** Winter SAT anomalies in the Arctic-Eurasian region (CI = 0.5 K SD^{-1}) in the ESO12 years (dots in Fig. 2b) regressed onto the preceding November ΔSST_{nNP} index (difference between the standardised SST_{cNP} and SST_{neNP} indices based on SSTs averaged over the cNP and neNP boxes in **a**, respectively). **d** As in **c** but for winter SAT anomalies regressed onto the preceding November SST_{cNP} index during the L1 subperiod (2004–

2012). In **a–d**, anomalies significant at $p = 0.05$ are shaded. **e** As in Fig. 2c but for correlation of the winter WACE$_\Delta$ index with the preceding November (blue) SST_{cNP} index, (red) ΔSST_{nNP} index, and (green) ΔSST_{sNP} index (difference between the standardised SST_{cNP} and SST_{seNP} indices based on SSTs averaged over the cNP and seNP boxes in **a**, respectively). **f** Comparison of (blue) the 15-year moving window correlation between the November SST_{cNP} index and the following winter WACE$_\Delta$ index with (red) the 15-year running mean of the raw (non-detrended) scaled (non-dimensional) autumn anomalies of (red) SST_{cNP} and (green) AMO

autumnal SST anomalies in the North Pacific is significant in the LATE but not the EARLY epoch, as shown for November (most significant) SST anomalies (Fig. 15a, b). In the LATE epoch, the WACE events are associated with anomalously warm SSTs in the central North Pacific surrounded by a "horseshoe" structure of anomalously cold SSTs to the north, east, and south (Fig. 15a). This structure is accompanied by a weak La Niña signal in the eastern equatorial Pacific and resembles the negative phase of the PDO (Mantua et al. 1997). Although not significant, the corresponding pattern for the EARLY epoch is similar (Fig. 15b).

The recent emergence of a strong linkage of the WACE pattern to the Pacific SST variability is further illustrated in Fig. 15e showing the 9-year moving window correlation of the winter WACE index with three November indices of this variability: SST_{cNP}, ΔSST_{nNP}, and ΔSST_{sNP}. The SST_{cNP} index represents SST anomalies in the central North Pacific

(averaged over the cNP box in Fig. 15a), whereas the "northern dipole" index ($\Delta SST_{nNP} = SST_{cNP} - SST_{neNP}$) and the "southern dipole" index ($\Delta SST_{sNP} = SST_{cNP} - SST_{seNP}$) are defined as the difference between these anomalies and the corresponding anomalies averaged over the north-eastern and the south-eastern North Pacific (neNP and seNP boxes in Fig. 15a), respectively. For the SSTs in the central North Pacific (blue curve) and the northern dipole (red curve), r_9 attains a maximum (> 0.9) around the window 2008 ± 4 including all strong LATE WACE events (L1 in Fig. 2b) and the window 2012 ± 4, respectively. For the southern dipole, the values of r_9 are somewhat lower (Fig. 15e, green curve), but its correlation with the WACE index over the entire LATE epoch is higher ($r = 0.81$). Over the entire ESO period, a considerable fraction (64%) of the variance of the strong WACE/CAWE events is explained by the northern

dipole index. Such strong associations of winter WACE variability with Pacific SST anomalies in November are captured neither by the canonical PDO index nor by the NINO3 index of equatorial SST variability (Table 3).

The winter SAT anomaly pattern associated with the preceding November SST variability in the North Pacific for the ESO12 years exhibits significant midlatitude anomalies in both Asia and the Mediterranean region (Fig. 15c). In the latter region, cold anomalies associated with warming events in the central North Pacific are particularly strong during the L1 subperiod (Fig. 15d) when they result from cold-air advection on the south-eastern rim of an anomalous anticyclone over the North Atlantic (Fig. 14d). Since significant cooling in the Mediterranean region on the rim of this anticyclone is also associated with October air-sea heat exchanges in the Arctic (Figs. 13f, 14b), the recent WACE variability should depend on autumn-to-winter Arctic-Pacific teleconnections. Such teleconnections are also

indicated by the resemblance between the winter anomaly patterns of Z_{300}^* during L1 associated with the November SST_{cNP} index (Fig. 14c) and October THF anomalies in the Arctic (Fig. 14a), with the area-weighted pattern correlation coefficient of 0.96. A similarly strong linkage ($r = 0.98$) is found between the November anomaly patterns of Z_{50} associated with the October THFs in the Arctic (Fig. 12d) and the November SST_{cNP} index (not shown). This result is in line with studies showing that the negative phase of the interannual component of the PDO tends to intensify the stratospheric polar vortex via impeding planetary waves from propagating into the stratosphere (Woo et al. 2015; Hu and Guan 2018). However, these studies focused on wintertime conditions. If the autumnal intensification of the stratospheric polar vortex drives the winter WACE pattern, its lagged downward influence should generate a positve NAO-like circulation anomaly accompanied by the Ural blocking pattern in the upper troposphere. However, investigation of
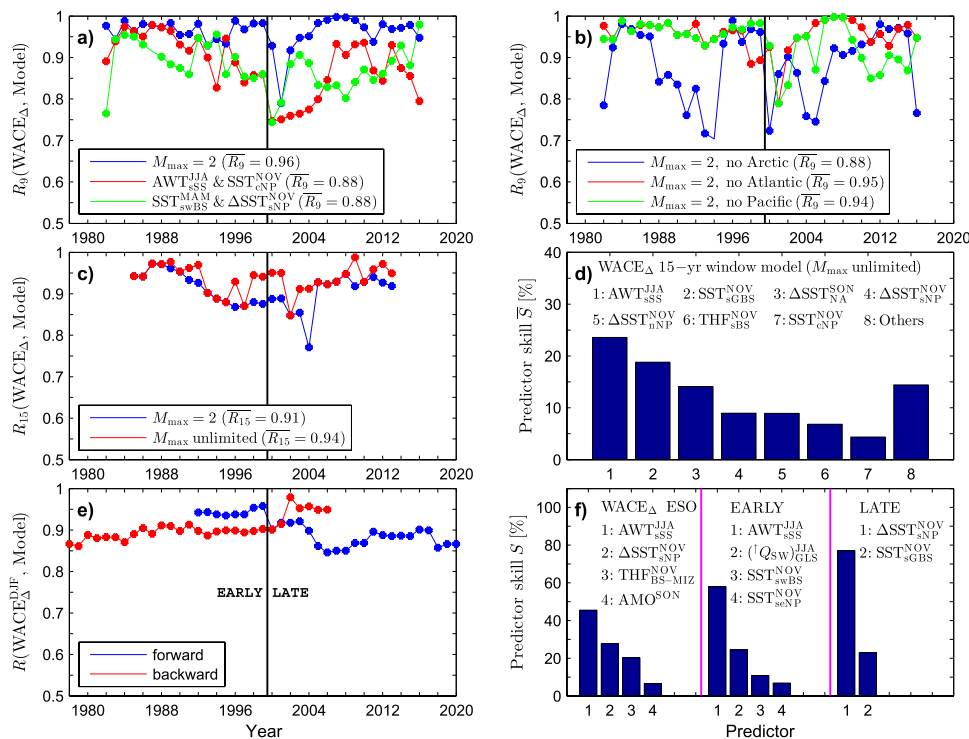
Fig. 16 a 9-year moving window correlation (R_9) of the winter WACE$_\Delta$ index (blue curve in Fig. 2b) with its MLR model fitted to (blue) not more than two optimal predictors selected by the model ($M_{max} = 2$ model) from those listed in Table 3, (red) the summer AWT$_{sSS}$ and November SST$_{cNP}$ indices as predictors, and (green) the spring SST$_{swBS}$ and November ΔSST$_{sNP}$ indices as predictors. The model is applied independently for each window to the window-detrended predictand and predictors. R_9 is plotted at the window's central year. Colour dots indicate values significant at $p = 0.05$. **b** As the blue curve in **a** but for the model with (blue) all Arctic, (red) all Atlantic, and (green) all Pacific predictors excluded. **c** As the blue curve in **a** but for the 15-year moving window correlation (R_{15}) for

(blue) the $M_{max} = 2$ model and (red) the M_{max}-unlimited model in which the maximum number of optimal predictors is not limited. **d** Relative average skill of the seven most important WACE$_\Delta$ predictors from the 15-year moving window M_{max}-unlimited model. **e** Correlation (R) of the WACE$_\Delta$ index with its M_{max}-unlimited model for the periods beginning at (blue) the first and (red) the last year of the time series and ending at the year successively moved forward and backward, respectively, starting from the 15-year-long initial period. R is plotted at the year of the moving end of the model period. **f** Relative fitting skill of the model-selected predictors from the M_{max}-unlimited WACE$_\Delta$ model for (left to right) the ESO period, the EARLY epoch, and the LATE epoch

whether this was indeed the case in the LATE epoch and whether the Pacific or the Arctic precursors were critical in setting up the stratospheric bridge is beyond the scope of this study. Other precursors, such as October snow cover anomalies in Eurasia, might have also contributed (Xu et al. 2018).

Winter Arctic warming and its influence on midlatitude atmospheric circulation may be modulated by the concurrent PDO phase (Screen and Francis 2016; Simon et al. 2022; Luo et al. 2022a). However, the recent enhancement of the winter WACE linkage to autumnal SSTs in the North Pacific is rather related to large-scale changes in ocean temperatures through the ESO period. This conjecture, if not biased by the fixed-area averaging of the data, is supported by a close correspondence between the 15-year moving window correlation of the winter WACE index with November SST anomalies in the central North Pacific and the 15-year running means of the raw autumn indices of SST variability in the North Atlantic (AMO index) and the central North Pacific itself (Fig. 15f).

5 WACE statistical model

Above, we identified several oceanic precursors of the winter WACE pattern and demonstrated that it is useless to try to explain its variability using any single precursor because the most important precursors either lose or gain significance over time. However, when combined, these precursors explain most of the WACE signal. This effect is illustrated in Fig. 16a, in which the blue curve shows the 9-year moving window correlation (R_9) of the WACE index with its 9-year moving window MLR model based on stepwise selection of up to two best predictors ($M_{max} = 2$ model) from the large set of Arctic, Atlantic, and Pacific precursors (listed in Table 3) using an adjusted R^2 criterion with FDR control (see Sect. 2.3 for details). The correlation is significant for all windows in the ESO period, and its average value over this period ($\overline{R_9}$) is remarkably high (0.96). The sensitivity experiments with the $M_{max} = 2$ model in which all Arctic, Atlantic, and Pacific predictors are in turn excluded indicate that (1) the Arctic predictors are most efficient in explaining the WACE variability in the ESO period, (2) the Atlantic predictors provide some independent information only at the end of the EARLY epoch, and (3) the Pacific predictors provide some independent information in the LATE epoch (Fig. 16b). These findings could be expected from comparison of the bivariate correlations (Figs. 8e, 9g, 10f, 15e), which also suggest a complementarity between the summer/ spring indices of Arctic climate variability related to the reemergence of SST anomalies and the November indices of PDO-like SST anomalies in the Pacific in explaining the

winter WACE variability. This complementarity is illustrated by the red and green curves in Fig. 16a showing the 9-year moving window correlation of the WACE index with its MLR model for two exemplary pairs of prescribed Arctic-Pacific predictors, a pair (AWT$_{sSS}^{JJA}$-SST$_{cNP}^{NOV}$) representing subsurface and surface ocean temperatures and a pair (SST$_{swBS}^{MAM}$-ΔSST$_{sNP}^{NOV}$) representing only SSTs. For both pairs, R_9 is significant for all windows. Its average value is equally high (0.88), indicating that the WACE variability is potentially predictable from satellite observations alone.

Only a very few predictors are needed for an efficient fit of the WACE variability also when the model window width is increased from 9 to 15 years. This is demonstrated in Fig. 16c showing the 15-year moving window correlation (R_{15}) of the WACE index with its two 15-year moving window models, the $M_{max} = 2$ model and the M_{max}-unlimited model in which no upper bound on the number of predictors that pass the adjusted R^2 criterion and the FDR control is imposed. Both models show good overall performance ($\overline{R_{15}} > 0.9$). For the M_{max}-unlimited model, the relative predictor importance (window-averaged predictor skill $\overline{S}$ in increasing R^2; see Sect. 2.3 for details) is reported in Fig. 16d for the seven most important predictors. The three most skillful ones are the summer AWT and November SST anomalies in the Arctic (AWT$_{sSS}^{JJA}$ and SST$_{swBS}^{NOV}$) and the autumn index of dipolar SST variability in the North Atlantic (ΔSST$_{NA}^{SON}$). The complementary influences are distributed mainly among Pacific predictors (ΔSST$_{sNP}^{NOV}$, ΔSST$_{nNP}^{NOV}$, and SST$_{cNP}^{NOV}$).

Because the WACE variability is significantly related to different precursors in the EARLY and LATE epochs, while the MLR model minimises the sum of the squared residuals over the entire fitted period, the efficiency of the WACE MLR model somewhat decreases with increasing time window width. However, this efficiency remains relatively high for any ESO subperiod, which is demonstrated in Fig. 16e showing the correlation R of the WACE index with its M_{max}-unlimited model applied over the time span successively extended forward and backward, starting from the first and the last 15-year-long subperiod, respectively. The value of R for the year 2020 on the blue curve and the year 1978 on the red curve corresponds to the correlation for the model for the entire ESO period ($R = 0.87$). The first value on these curves to the left and to the right of the black vertical line represents the correlation for the model for the EARLY ($R = 0.95$) and the LATE ($R = 0.90$) epoch, respectively. For these three periods, the relative fitting skill of the predictors selected by the model is shown in Fig. 16f. In the case of the ESO period, the model retains four predictors. The two most important ones are the summer AWT anomalies in the Arctic (AWT$_{sSS}^{JJA}$, $S = 45.5\%$) and the southern dipole

Fig. 17 As in (*left*) Fig. 16e and (*right*) Fig. 16f but for four other winter predictands from Table 1: (**a**, **b**) sea ice area in the Greenland–Barents Seas region (SIA_{GBS} index), (**c**, **d**) surface air temperature in this region (SAT_{GBS} index), (**e**, **f**) surface air temperature in mid-latitude Eurasia (SAT_{mE} index), and (**g**, **h**) sea level pressure in the Ural-Siberian High region (SLP_{USH} index)
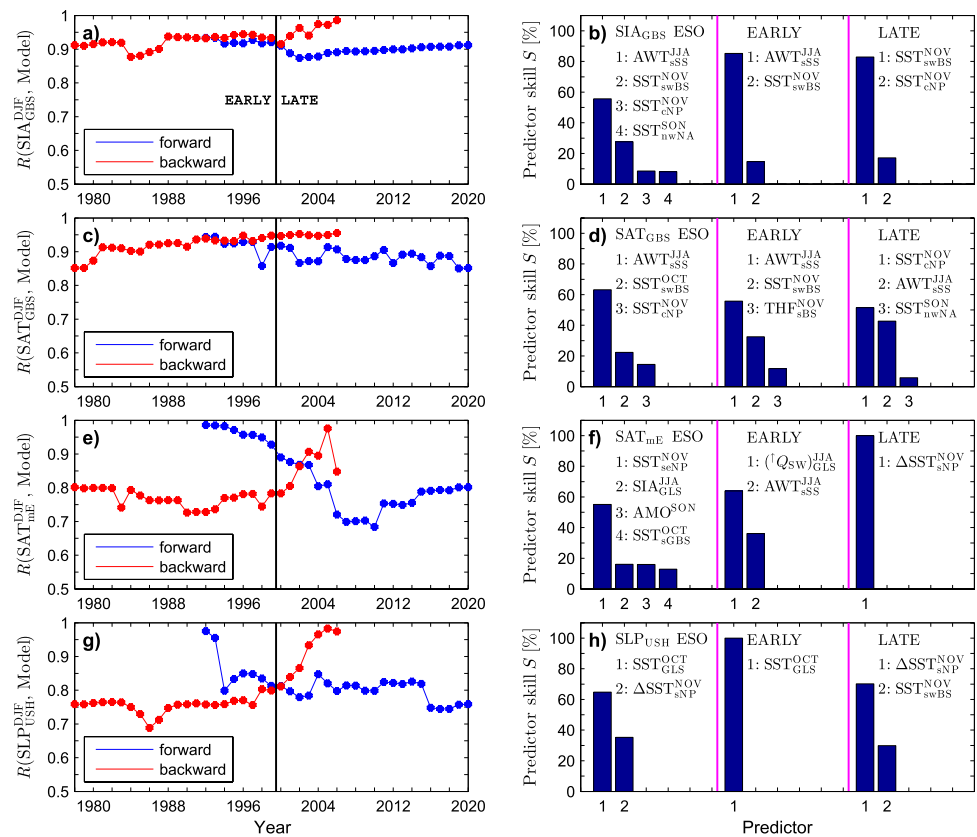
index of November North Pacific SST variability (ΔSST_{sNP}^{NOV}, $S = 27.7\%$). The model selects four predictors also for the EARLY epoch. The two most skillful ones represent Arctic summer anomalies of subsurface ocean temperature (AWT_{sSS}^{JJA}, $S = 58.0\%$) and surface upward shortwave radiation [($^\uparrow Q_{SW})_{GLS}^{JJA}$, $S = 24.4\%$]. Only two predictors contribute to the model for the LATE epoch. Both represent November SST variability, the more skillful one in the North Pacific (ΔSST_{sNP}^{NOV}, $S = 77\%$) and the less skillful one in the Arctic (SST_{sGBS}^{NOV}, $S = 33\%$).

A high potential predictability is found not only for the WACE anomaly but also for several related indicators of winter climate variability, which is demonstrated in Fig. 17 for a set of four predictands selected from Table 1, representing Arctic sea ice anomalies (SIA_{GBS} index), SAT anomalies over the Arctic and Eurasian lobes of the WACE pattern (SAT_{GBS} and SAT_{mE} indices), and SLP anomalies in Eurasia (SLP_{USH} index). The figure shows the correlations of the given predictand with its MLR M_{max}-unlimited model in the forward and backward extending period configurations (left panels) and the relative fitting skill of the model-selected predictors for the ESO, EARLY, and LATE periods (right panels). The most stable is the model for the SIA predictand, for which the fit with 2–4 predictors explains 83–85% of the variance ($R > 0.9$) for each of these periods. For the EARLY epoch, the model fits all predictands to Arctic predictors.

Three, two, and one of these predictors account for 84, 86, and 66% of the variance of SAT_{GBS}, SAT_{mE}, and SLP_{USH}, respectively. For the LATE epoch, the model with three predictors from different regions explains a large fraction (90%) of the variance of the Arctic SAT predictand. A somewhat lower fraction of the variance of the Eurasian SAT (61%) and SLP (66%) predictands is explained by the model with one (Pacific) and two (one Pacific and one Arctic) predictors, respectively. However, when the LATE epoch is shortened by a few years, e.g., to cover the recent period since 2003, the model is very efficient ($R > 0.9$) also for the Eurasian predictands.

6 Summary and conclusions

A remarkable recurrent feature of winter climate variability that has recently attracted great scientific attention is the "warm Arctic-cold Eurasia" (WACE) dipole pattern of opposite sign anomalies of surface air temperature (SAT) in the Barents Sea region and midlatitude Eurasia (Overland et al. 2011; Mori et al. 2014; Luo et al. 2016; Zhao et al. 2023). Many studies have analysed the WACE linkage to changing surface conditions in the Arctic based on simultaneous relationships, while lagged relationships have been addressed to

a lesser extent, mainly in relation to autumnal sea ice anomalies. Similarly, inferences about WACE teleconnections to surface conditions in the North Atlantic or the Pacific Ocean have usually been made from simultaneous relationships, often in the context of decadal-to-multidecadal variability (Jin et al. 2020; Luo et al. 2022a). Studies of winter WACE linkages to ocean temperatures in the preceding seasons are practically non-existent. Based on data from a 24-year-long period, one study showed a significant WACE-like dipole of wintertime SAT variability associated with summertime Atlantic water temperature (AWT) anomalies in the Barents Sea (Schlichtholz 2016). Using detrended observations and reanalysis data, the present study investigates statistical relationships of the interannual variability in the winter (December–January–February) mean WACE pattern to the concurrent anomalies of atmospheric circulation and oceanic precursors during a longer period, covering the era of satellite observations (ESO) from the winter of 1978/79 to the winter of 2020/21, and its different subperiods. For the first time, a potentially high seasonal predictability of winter WACE variability is demonstrated by applying lead-lag correlation analysis and a multiple linear regression (MLR) model to a holistic set of predictors, including, in addition to summer AWT anomalies in the Barents Sea, seasonal or monthly mean indices of variability in sea surface temperature (SST), sea ice concentration (SIC), and surface turbulent heat flux (THF) in the Eurasian Arctic and SST in the North Atlantic and the Pacific Ocean.

The WACE intensity is represented by its index based on the difference between the SATs averaged over significant lobes of the canonical WACE pattern. Positive values of this index correspond to WACE events, and negative values correspond to "cold Arctic-warm Eurasia" (CAWE) events. Twelve strong WACE/CAWE events are identified, with a magnitude of the WACE index greater than one standard deviation. Then, a close relationship of these events ($|r| > 0.9$) with concurrent climatic anomalies, such as those of the ice-covered area in the Eurasian Arctic, the sea level pressure (SLP) in the Ural-Siberian High region, the strength of upper tropospheric westerlies over northern Eurasia, and a quasi-stationary wavenumber-1 planetary wave in high latitudes, is highlighted. The centres of action of this wave form a quadripole with the centres of action of a midlatitude wave. During its positive phase, this quadripole resembles an atmospheric circulation anomaly (Ural blocking pattern accompanied by a positive North Atlantic Oscillation dipole) that promotes WACE amplification through feedbacks between sea ice loss in the Barents Sea region, weakened westerlies over Eurasia, and enhanced Ural blocking activity (Luo et al. 2016; Yao et al. 2017; Gong and Luo 2017). Refined analysis based on 9-year moving window correlations shows that maximum out-of-phase covariability between the Arctic and Eurasian SATs occurred at the

beginning of the ESO period (E1 subperiod) and around the late 2000s (L1 subperiod). During both subperiods, the upper tropospheric high-latitude planetary wave was closely related to the midlatitude wave and to the surface wind cyclonicity in the Arctic. All strong WACE events occurred in these two subperiods. A higher number of these events during L1 (four) than during E1 (two) is consistent with the increased persistence of Ural blocking in the LATE epoch of the ESO period (since 2000) than in its EARLY epoch (before 2000) demonstrated by Luo et al. (2016). However, a stronger WACE link to SIC anomalies is found during E1 than during L1.

A notable feature of winter WACE events is their stronger association with a decrease in ocean heat loss to the atmosphere on the open water side of the ice edge than with an increase in atmospheric heat gain over the area of reduced sea ice cover in the Eurasian Arctic. In some studies, this feature was considered as an indicator of a negligible influence of Arctic surface forcing on Eurasian SATs (Sorokina et al. 2016; Blackport et al. 2019), which is disputable in light of the results presented here. Much of the winter WACE variability and associated atmospheric circulation anomalies during the ESO period are shown to be explained by anomalous ocean temperatures and air-sea heat exchanges in the Eurasian Arctic during the preceding months. In particular, summer AWT anomalies and autumnal SST anomalies in this region explain about 70–80% of the variance of the following winter WACE variability and SLP anomalies in the Ural-Siberian High region during the strong WACE/ CAWE events.

Jang et al. (2021) showed that linkages of winter SAT variability in midlatitude Eurasia to autumn Arctic SIC anomalies are conditioned by the type of autumnal atmospheric circulation. Here, we find a somewhat stronger linkage of this variability to summer SIC anomalies (and associated changes in surface upward shortwave radiation) than to autumn SIC anomalies. However, this linkage was suppressed in the LATE epoch. A substantial recent deterioration is also found for the winter WACE linkage to the preceding summer AWT and spring SST anomalies but not to autumn SST anomalies in the Barents Sea. Further analysis reveals that during the two subperiods of maximum covariability between the Arctic and Eurasian SATs, the WACE events were preceded by a significantly increased autumnal ocean heat loss to the atmosphere in the Eurasian Arctic. About 90% of the variance of the winter WACE index can be explained by autumnal THF anomalies in open water during E1 and in the marginal ice zone during L1. This geographical difference could be one of the reasons why a robust link of the winter WACE pattern to the preceding autumn THF anomalies in the Eurasian Arctic was not identified in an earlier study from regressions over a period including both subperiods (Sorokina et al. 2016). It is also

found that the anomalous autumnal ocean heat loss could contribute to the winter WACE events via a stratospheric pathway involving a shift of the polar vortex in E1 and its intensification in L1.

Analysis of SST variability in the Arctic-North Atlantic region in different seasons reveals that the winter WACE linkage to the summer AWT anomalies in the Barents Sea may reflect an atmospheric response to a coherent large-scale surface reemergence of ocean temperature anomalies. When the WACE events are preceded by warm springtime SST and summer AWT anomalies in the Eurasian Arctic, they are also preceded by springtime and autumn SST anomalies in the extratropical North Atlantic, warm in the Gulf Stream extension region and cold in the Labrador Sea and adjacent areas. This linkage had been robust only until the early 2000s. In the LATE epoch, the winter WACE variability has not been significantly related to springtime SSTs in the Eurasian Arctic or autumnal SSTs in the North Atlantic. These results put into a broader perspective the findings from earlier studies indicating that the WACE pattern may be related to an amplification of Arctic warming in the Barents-Kara Seas region through processes dependent on SST anomalies in the Gulf Stream region (Sato et al. 2014; Jung et al. 2017; Luo et al. 2019a). These studies investigated neither seasonally delayed linkages nor changes over time in the relationships they highlighted.

It is also demonstrated that, since the early 2000s, the winter WACE variability has been strongly related to autumnal surface conditions in the North Pacific. The WACE events were preceded by an SST anomaly pattern that resembles the negative phase of the Pacific Decadal Oscillation (PDO). The winter anomaly patterns of atmospheric circulation associated with autumnal Pacific SST anomalies during the L1 subperiod are strikingly similar to the corresponding patterns associated with autumnal air-sea heat exchanges in the Eurasian Arctic, indicating a recent strengthening of autumn-to-winter Arctic-Pacific teleconnections shaping the WACE variability. The tropospheric and stratospheric pathways involved in these teleconnections require further investigation. Further investigation is also warranted to determine the cause of the recent flip-flop in the WACE teleconnections (deterioration of the winter WACE link to reemerging SST anomalies in the Arctic-North Atlantic region in congruence with enhancement of its link to autumnal SST anomalies in the North Pacific). This flip-flop could result from changing background climate conditions, an atmospheric manifestation of which is the enhanced wintertime covariability between the Ural and North Pacific blocking highs since the early 2000s (Zhao et al. 2022). A remarkable coincidence of this flip-flop with ocean warming in the Eurasian Arctic, North Atlantic, and central North Pacific through the ESO period is evidenced here. This coincidence suggests that the flip-flop might have been caused by modulatory effects of the Atlantic Multidecadal Oscillation and the Interdecadal Pacific Oscillation, which are the modes of climate variability previously shown to influence decadal changes in global surface temperature (Dai et al. 2015) and the WACE pattern itself (Luo et al. 2022b).

Since the most important WACE precursors are complementary and sufficiently significant, their combination explains most of the WACE variability. Using the MLR model in different configurations, a potentially high seasonal predictability is demonstrated not only for the WACE dipole but also for several related winter climatic anomalies, including those of the SATs over the Arctic and Eurasian lobes of the WACE pattern. Potential caveats of the present study include the use of (1) still relatively short time series, (2) a relatively low-resolution atmospheric (NCEP/NCAR) reanalysis, and (3) data averaged over fixed areas to represent dynamic and changing climatic patterns and features. An advantage of the selected period is that observational SIC/SST datasets from that period are more reliable than earlier SIC/SST observations because they include information from continuous satellite measurements. Moreover, during the ESO period, the SAT anomalies from the NCEP/NCAR reanalysis averaged over the Arctic and Eurasian lobes of the WACE pattern are highly consistent with the Berkeley Earth surface temperature record. Despite their limitations, the findings of this study should provide valuable information to the debate on the Arctic-midlatitude climate linkages and a useful benchmark for complex dynamic seasonal forecast systems. They may also inspire dedicated climate-modelling studies or analysis of existing climate-model simulations to further explore the mechanisms behind the statistical relationships identified here.

Declarations

References

Alexeev VA, Ivanov VV, Kwok R, Smedsrud LH (2013) North Atlantic warming and declining volume of arctic sea ice. Cryosphere Discuss 7(1):245–265. https://doi.org/10.5194/tcd-7-245-2013

Årthun M, Eldevik T, Smedsrud LH, Skagseth Ø, Ingvaldsen RB (2012) Quantifying the influence of Atlantic heat on Barents Sea ice variability and retreat. J Clim 25:4736–4743

Bar-Gera H (2017) The target parameter of adjusted R-squared in fixed-design experiments. Am Stat 71(2):112–119. https://doi.org/10.1080/00031305.2016.1200489

Barnston AG, Livezey RE (1987) Classification, seasonality and persistence of low-frequency atmospheric circulation patterns. Mon Weather Rev 115(6):1083–1126. https://doi.org/10.1175/1520-0493(1987)115<1083:CSAPOL>2.0.CO;2

Beer E, Eisenman I, Wagner TJW (2020) Polar amplification due to enhanced heat flux across the halocline. Geophys Res Lett 47(4):e2019GL086706. https://doi.org/10.1029/2019GL086706

Behrendt A, Sumata H, Rabe B, Schauer U (2018) UDASH—unified database for arctic and subarctic hydrography. Earth Syst Sci Data 10(2):1119–1138. https://doi.org/10.5194/essd-10-1119-2018

Bengtsson L, Semenov VA, Johannessen OM (2004) The early twentieth-century warming in the Arctic—a possible mechanism. J Clim 17:4045–4057

Benjamini Y, Yekutieli D (2001) The control of the false discovery rate in multiple testing under dependency. Ann Stat 29(4):1165–1188. https://doi.org/10.1214/aos/1013699998

Bintanja R, Graversen RG, Hazeleger W (2011) Arctic winter warming amplified by the thermal inversion and consequent low infrared cooling to space. Nat Geosci 4(11):758–761. https://doi.org/10.1038/ngeo1285

Blackport R, Screen JA, van der Wiel K et al (2019) Minimal influence of reduced Arctic sea ice on coincident cold winters in mid-latitudes. Nat Clim Change 9:697–704. https://doi.org/10.1038/s41558-019-0551-4

Bretherton CS, Widmann M, Dymnikov VP, Wallace JM, Blade I (1999) The effective number of spatial degrees of freedom of a time-varying field. J Clim 12(7):1990–2009

Bushuk M, Msadek R, Winton M, Vecchi GA, Gudgel R, Rosati A, Yang X (2017) Skillful regional prediction of Arctic sea ice on seasonal timescales. Geophys Res Lett 44(10):4953–4964. https://doi.org/10.1002/2017GL073155

Bushuk M, Yang X, Winton M, Msadek R, Harrison M, Rosati A, Gudgel R (2019) The value of sustained ocean observations for sea ice predictions in the Barents Sea. J Clim 32(20):7017–7035. https://doi.org/10.1175/JCLI-D-19-0179.1

Cai Z, You Q, Chen HW, Zhang R, Zuo Z, Dai G, Chen D, Cohen J, Zolina O, Gulev SK (2023) Interdecadal variability of the warm Arctic-cold Eurasia pattern linked to the Barents oscillation. Atmos Res 287:106712. https://doi.org/10.1016/j.atmosres.2023.106712

Chen Y, Luo D, Zhong L (2021) North Atlantic multidecadal footprint of the recent winter warm Arctic-cold Siberia pattern. Clim Dyn 57:121–139. https://doi.org/10.1007/s00382-021-05698-9

Cho DJ, Kim KY (2021) Role of Ural blocking in Arctic sea ice loss and its connection with Arctic warming in winter. Clim Dyn 56:1571–1588. https://doi.org/10.1007/s00382-020-05545-3

Chung ES, Ha KJ, Timmermann A, Stuecker MF, Bodai T, Lee SK (2021) Cold-season Arctic amplification driven by Arctic ocean-mediated seasonal energy transfer. Earth's Future 9(2):e2020EF001898. https://doi.org/10.1029/2020EF001898

Chylek P, Folland CK, Lesins G, Dubey MK, Wang M (2009) Arctic air temperature change amplification and the Atlantic Multidecadal Oscillation. Geophys Res Lett 36(14):L14801. https://doi.org/10.1029/2009gl038777

Cohen J, Screen JA, Furtado JC, Barlow M, Whittleston D, Coumou D, Francis J, Dethloff K, Entekhabi D, Overland J, Jones J (2014) Recent Arctic amplification and extreme mid-latitude weather. Nat Geosci 7:627–637. https://doi.org/10.1038/ngeo2234

Cohen J, Zhang X, Francis J et al (2020) Divergent consensuses on Arctic amplification influence on midlatitude severe winter weather. Nat Clim Change 10:20–29. https://doi.org/10.1038/s41558-019-0662-y

Comiso JC (2017) Bootstrap sea ice concentrations from Nimbus-7 SMMR and DMSP SSM/I-SSMIS, Version 3 [Northern Hemisphere, November 1978 to February 2018]. NASA National Snow and Ice Data Center Distributed Active Archive Center, Boulder, Colorado USA. https://doi.org/10.5067/7Q8HCCWS4I0R. Accessed 29 Jan 2021

Dai A, Song M (2020) Little influence of Arctic amplification on midlatitude climate. Nat Clim Change 10:231–237. https://doi.org/10.1038/s41558-020-0694-3

Dai A, Deng J (2022) Recent Eurasian winter cooling partly caused by internal multidecadal variability amplified by Arctic sea ice-air interactions. Clim Dyn 58:3261–3277. https://doi.org/10.1007/s00382-021-06095-y

Dai A, Jenkins MT (2023) Relationships among Arctic warming, sea-ice loss, stability, lapse rate feedback, and Arctic amplification. Clim Dyn. https://doi.org/10.1007/s00382-023-06848-x

Dai A, Fyfe JC, Xie SP, Dai X (2015) Decadal modulation of global surface temperature by internal climate variability. Nat Clim Change 5:555–559. https://doi.org/10.1038/nclimate2605

Dai A, Luo D, Song M, Liu J (2019) Arctic amplification is caused by sea-ice loss under increasing CO2. Nat Commun 10:121. https://doi.org/10.1038/s41467-018-07954-9

Deng J, Dai A (2022) Sea ice-air interactions amplify multidecadal variability in the North Atlantic and Arctic region. Nat Commun 13:2100. https://doi.org/10.1038/s41467-022-29810-7

Deser C, Alexander MA, Timlin MS (2003) Understanding the persistence of sea surface temperature anomalies in midlatitudes. J Clim 16:57–72

Deser C, Tomas RA, Peng S (2007) The transient atmospheric circulation response to North Atlantic SST and sea ice anomalies. J Clim 20:4751–4767. https://doi.org/10.1175/JCLI4278.1

Fang M, Li X, Chen H et al (2022) Arctic amplification modulated by Atlantic Multidecadal Oscillation and greenhouse forcing on multidecadal to century scales. Nat Commun 13:1865. https://doi.org/10.1038/s41467-022-29523-x

Furevik T (2001) Annual and interannual variability of Atlantic Water temperatures in the Norwegian and Barents Seas. Deep-Sea Res Part I 48(2):383–404. https://doi.org/10.1016/S0967-0637(00)00050-9

Gong T, Luo D (2017) Ural blocking as an amplifier of the Arctic sea ice decline in winter. J Clim 30:2639–2654. https://doi.org/10.1175/JCLI-D-16-0548.1

Gu Q, Gervais M (2021) Exploring North Atlantic and North Pacific decadal climate prediction using self-organizing maps. J Clim 34(1):123–141. https://doi.org/10.1175/JCLI-D-20-0017.1

Harris CL, Plueddemann AJ, Gawarkiewicz G (1998) Water mass distribution and polar front structure in the western Barents Sea. J Geophys Res 103(C2):2905–2917

Helland-Hansen B, Nansen F (1909) The Norwegian Sea: its physical oceanography based upon the Norwegian researches 1900–1904. Rep Norw Fish Mar Inv 2(2):1–360

Herbaut C, Houssais MN, Close S, Blaizot AC (2015) Two wind-driven modes of winter sea ice variability in the Barents Sea. Deep-Sea Res Part I 106:97–115. https://doi.org/10.1016/j.dsr.2015.10.005

Honda M, Inoue J, Yamane S (2009) Influence of low Arctic sea ice minima on anomalously cold Eurasian winter. Geophys Res Lett 36:L08707. https://doi.org/10.1029/2008GL037079

Hu D, Guan Z (2018) Decadal relationship between the stratospheric Arctic vortex and pacific decadal oscillation. J Clim 31(9):3371–3386. https://doi.org/10.1175/JCLI-D-17-0266.1

Huang B, Thorne PW, Banzon VF, Boyer T, Chepurin G, Lawrimore JH, Menne MJ, Smith TM, Vose RS, Zhang HM (2017a) NOAA extended reconstructed sea surface temperature (ERSST), Version 5 [February 1978 to February 2021]

Huang J, Zhang X, Zhang Q, Lin Y, Hao M, Luo Y, Zhao Z, Yao Y, Chen X, Wang L, Nie S, Yin Y, Xu Y, Zhang J (2017b) Recently amplified arctic warming has contributed to a continual global warming trend. Nat Clim Change 7:875–879. https://doi.org/10.1038/s41558-017-0009-5

ICES (2021) Hydrographic Database. International Council for the Exploration of the Sea, Copenhagen. http://ocean.ices.dk/HydChem/HydChem.aspx

Inoue J, Hori ME, Takaya K (2012) The role of Barents Sea ice in the wintertime cyclone track and emergence of a warm-Arctic cold-Siberian anomaly. J Clim 25:2561–2568

Jang YS, Jun SY, Son SW, Min SK, Kug JS (2021) Delayed impacts of Arctic sea-ice loss on Eurasian severe cold winters. J Geophys Res: Atmos 126(23):e2021JD035286. https://doi.org/10.1029/2021JD035286

Jin C, Wang B, Yang YM, Liu J (2020) "Warm Arctic-Cold Siberia'' as an internal mode instigated by North Atlantic warming. Geophys Res Lett 47(9):e2019GL086248. https://doi.org/10.1029/2019GL086248

Jung O, Sung MK, Sato K, Lim YK, Kim SJ, Baek EH, Jeong JH, Kim BM (2017) How does the SST variability over the western North Atlantic Ocean control Arctic warming over the Barents-Kara Seas? Environ Res Lett 12(3):034021

Kalnay E, Kanamitsu M, Kistler R, Collins W, Deaven D, Gandin L, Iredell M, Saha S, White G, Woollen J, Zhu Y, Chelliah M, Ebisuzaki W, Higgins W, Janowiak J, Mo KC, Ropelewski C, Wang J, Leetmaa A, Reynolds R, Jenne R, Joseph D (1996) The NCEP/NCAR 40-yr reanalysis project. Bull Amer Meteor Soc 77:437–471

Kim KY, Son SW (2016) Physical characteristics of Eurasian winter temperature variability. Environ Res Lett 11(4):044009. https://doi.org/10.1088/1748-9326/11/4/044009

Kim HJ, Son SW (2020) Eurasian winter temperature change in recent decades and its association with Arctic sea ice loss. Polar Res 39:1. https://doi.org/10.33265/polar.v39.3363

Kim BM, Son SW, Min SK, Jeong JH, Kim SJ, Zhang X, Shim T, Yoon JH (2014) Weakening of the stratospheric polar vortex by Arctic sea-ice loss. Nat Commun 5:4646. https://doi.org/10.1038/ncomms5646

Kim KY, Kim JY, Kim J, Yeo S, Na H, Hamlington BD, Leben RR (2019) Vertical feedback mechanism of winter Arctic amplification and sea ice loss. Sci Rep 9:1184. https://doi.org/10.1038/s41598-018-38109-x

Kim HJ, Son SW, Moon W, Kug JS, Hwang J (2021) Subseasonal relationship between Arctic and Eurasian surface air temperature. Sci Rep 11:4081. https://doi.org/10.1038/s41598-021-83486-5

Kug JS, Jeong JH, Jang YS, Kim BM, Folland CK, Min SK, Son SW (2015) Two distinct influences of Arctic warming on cold winters over North America and East Asia. Nat Geosci 8:759–762. https://doi.org/10.1038/ngeo2517

Lee S, Gong T, Feldstein SB, Screen JA, Simmonds I (2017) Revisiting the cause of the 1989–2009 Arctic surface warming using the surface energy budget: downward infrared radiation dominates the surface fluxes. Geophys Res Lett 44(20):10,654-10,661. https://doi.org/10.1002/2017GL075375

Li D, Zhang R, Knutson TR (2017) On the discrepancy between observed and CMIP5 multi-model simulated Barents Sea winter sea ice decline. Nat Commun 8:14991. https://doi.org/10.1038/ncomms14991

Li F, Orsolini YJ, Wang H, Gao Y, He S (2018) Atlantic Multidecadal Oscillation modulates the impacts of Arctic sea ice decline. Geophys Res Lett 45(5):2497–2506. https://doi.org/10.1002/2017GL076210

Li M, Luo D, Simmonds I, Dai A, Zhong L, Yao Y (2021) Anchoring of atmospheric teleconnection patterns by Arctic Sea ice loss and its link to winter cold anomalies in East Asia. Int J Climatol 41:547–558. https://doi.org/10.1002/joc.6637

Lien VS, Schlichtholz P, Skagseth Ø, Vikebø FB (2017) Wind-driven Atlantic water flow as a direct mode for reduced Barents Sea ice cover. J Clim 30(2):803–812. https://doi.org/10.1175/JCLI-D-16-0025.1

Lind S, Ingvaldsen RB, Furevik T (2018) Arctic warming hotspot in the northern Barents Sea linked to declining sea-ice import. Nat Clim Change 8:634–639. https://doi.org/10.1038/s41558-018-0205-y

Luo D, Xiao Y, Yao Y, Dai A, Simmonds I, Franzke CLE (2016) Impact of Ural blocking on winter warm Arctic-cold Eurasian anomalies. Part I: blocking-induced amplification. J Clim 29(11):3925–3947. https://doi.org/10.1175/JCLI-D-15-0611.1

Luo B, Luo D, Wu L, Zhong L, Simmonds I (2017a) Atmospheric circulation patterns which promote winter Arctic sea ice decline. Environ Res Lett 12(5):054017. https://doi.org/10.1088/1748-9326/aa69d0

Luo D, Chen Y, Dai A, Mu M, Zhang R, Simmonds I (2017b) Winter Eurasian cooling linked with the Atlantic Multidecadal

Oscillation. Environ Res Lett 12(12):125002. https://doi.org/10.1088/1748-9326/aa8de8

Luo D, Yao Y, Dai A, Simmonds I, Zhong L (2017c) Increased quasi stationarity and persistence of winter Ural Blocking and Eurasian extreme cold events in response to Arctic warming. Part II: a theoretical explanation. J Clim 30(10):3569–3587. https://doi.org/10.1175/JCLI-D-16-0262.1

Luo D, Chen X, Dai A, Simmonds I (2018) Changes in atmospheric blocking circulations linked with winter Arctic warming: a new perspective. J Clim 31(18):7661–7678. https://doi.org/10.1175/JCLI-D-18-0040.1

Luo B, Luo D, Dai A, Simmonds I (2019a) The winter midlatitude-Arctic interaction: effects of North Atlantic SST and high-latitude blocking on Arctic sea ice and Eurasian cooling. Clim Dyn 52:2981–3004. https://doi.org/10.1007/s00382-018-4301-5

Luo D, Chen X, Overland J, Simmonds I, Wu Y, Zhang P (2019b) Weakened potential vorticity barrier linked to recent winter Arctic Sea ice loss and midlatitude cold extremes. J Clim 32:4235–4261. https://doi.org/10.1175/JCLI-D-18-0449.1

Luo B, Luo D, Dai A, Simmonds I, Wu L (2021) A connection of winter Eurasian cold anomaly to the modulation of Ural blocking by ENSO. Geophys Res Lett 48(17):e2021GL094304. https://doi.org/10.1029/2021GL094304

Luo B, Luo D, Dai A, Simmonds I, Wu L (2022a) Decadal variability of winter warm Arctic-cold Eurasia dipole patterns modulated by Pacific Decadal Oscillation and Atlantic Multidecadal Oscillation. Earth's Future 10(1):e2021EF002351. https://doi.org/10.1029/2021EF002351

Luo B, Luo D, Dai A, Simmonds I, Wu L (2022b) The modulation of Interdecadal Pacific Oscillation and Atlantic Multidecadal Oscillation on winter Eurasian cold anomaly via the Ural blocking change. Clim Dyn 59:127–150. https://doi.org/10.1007/s00382-021-06119-7

Luo B, Luo D, Ge Y, Dai A, Wang L, Simmonds I, Xiao C, Yao Y (2023) Origins of Barents-Kara sea-ice interannual variability modulated by the Atlantic pathway of El Niño-Southern Oscillation. Nat Comm 14:585. https://doi.org/10.1038/s41467-023-36136-5

Mantua N, Hare S, Zhang Y, Wallace J, Francis R (1997) A Pacific interdecadal climate oscillation with impacts on salmon production. Bull Am Meteor Soc 78:1069–1079

MathWorks (2014) MATLAB and Statistics Toolbox Release 2014a. The MathWorks Inc, Natick, Massachusetts, United States

Matsumura S, Kosaka Y (2019) Arctic-Eurasian climate linkage induced by tropical ocean variability. Nat Commun 10:3441. https://doi.org/10.1038/s41467-019-11359-7

Meier WN, Hovelsrud GK, van Oort BE, Key JR, Kovacs KM, Michel C, Haas C, Granskog MA, Gerland S, Perovich DK, Makshtas A, Reist JD (2014) Arctic sea ice in transformation: a review of recent observed changes and impacts on biology and human activity. Rev Geophys 52(3):185–217. https://doi.org/10.1002/2013RG000431

Messori G, Woods C, Caballero R (2018) On the drivers of wintertime temperature extremes in the high arctic. J Clim 31:1597–1618. https://doi.org/10.1175/JCLI-D-17-0386.1

Mori M, Watanabe M, Shiogama H, Inoue J, Kimoto M (2014) Robust Arctic sea-ice influence on the frequent Eurasian cold winters in past decades. Nat Geosci 7:869–873. https://doi.org/10.1038/ngeo2277

Mori M, Kosaka Y, Watanabe M, Nakamura H, Kimoto M (2019) A reconciled estimate of the influence of Arctic sea-ice loss on recent Eurasian cooling. Nat Clim Change 9(2):123–129. https://doi.org/10.1038/s41558-018-0379-3

Nakanowatari T, Sato K, Inoue J (2014) Predictability of the Barents Sea ice in early winter: remote effects of oceanic and atmospheric thermal conditions from the North Atlantic. J Clim 27(23):8884–8901. https://doi.org/10.1175/JCLI-D-14-00125.1

North GR, Bell TL, Cahalan RF, Moeng FJ (1982) Sampling errors in the estimation of empirical orthogonal functions. Mon Weather Rev 110:699–706

Onarheim IH, Eldevik T, Smedsrud LH, Stroeve JC (2018) Seasonal and regional manifestation of Arctic sea ice loss. J Clim 31(12):4917–4932. https://doi.org/10.1175/JCLI-D-17-0427.1

Overland J, Wood K, Wang M (2011) Warm Arctic–cold continents: climate impacts of the newly open Arctic Sea. Polar Res 30(1):15787. https://doi.org/10.3402/polar.v30i0.15787

Overland JE, Ballinger TJ, Cohen J, Francis JA, Hanna E, Jaiser R, Kim BM, Kim SJ, Ukita J, Vihma T, Wang M, Zhang X (2021) How do intermittency and simultaneous processes obfuscate the Arctic influence on midlatitude winter extreme weather events? Environ Res Lett 16(4):043002. https://doi.org/10.1088/1748-9326/abdb5d

Petoukhov V, Semenov VA (2010) A link between reduced Barents-Kara sea ice and cold winter extremes over northern continents. J Geophys Res 115:D21111. https://doi.org/10.1029/2009JD013568

Pithan F, Mauritsen T (2014) Arctic amplification dominated by temperature feedbacks in contemporary climate models. Nat Geosci 7(3):181–184. https://doi.org/10.1038/ngeo2071

Polyakov IV, Pnyushkov AV, Alkire MB, Ashik IM, Baumann TM, Carmack EC, Goszczko I, Guthrie J, Ivanov VV, Kanzow T, Krishfield R, Kwok R, Sundfjord A, Morison J, Rember R, Yulin A (2017) Greater role for Atlantic inflows on sea-ice loss in the Eurasian Basin of the Arctic Ocean. Science 356(6335):285–291. https://doi.org/10.1126/science.aai8204

Rantanen M, Karpechko AY, Lipponen A, Nordling K, Hyvärinen O, Ruosteenoja K, Vihma T, Laaksonen A (2022) The Arctic has warmed nearly four times faster than the globe since 1979. Commun Earth Environ 3:168. https://doi.org/10.1038/s43247-022-00498-3

Reynolds RW, Rayner NA, Smith TM, Stokes DC, Wang W (2002) An improved in situ and satellite SST analysis for climate. J Clim 15:1609–1625

Rohde RA, Hausfather Z (2020) The Berkeley earth land/ocean temperature record. Earth Syst Sci Data 12(4):3469–3479. https://doi.org/10.5194/essd-12-3469-2020

Rudeva I, Simmonds I (2021) Midlatitude winter extreme temperature events and connections with anomalies in the Arctic and tropics. J Clim 34(10):3733–3749. https://doi.org/10.1175/JCLI-D-20-0371.1

Sato K, Inoue J, Watanabe M (2014) Influence of the Gulf Stream on the Barents Sea ice retreat and Eurasian coldness during early winter. Environ Res Lett 9:084009. https://doi.org/10.1088/1748-9326/9/8/084009

Schlichtholz P (2011) Influence of oceanic heat variability on sea ice anomalies in the Nordic Seas. Geophys Res Lett 38:L05705. https://doi.org/10.1029/2010GL045894

Schlichtholz P (2013) Observational evidence for oceanic forcing of atmospheric variability in the Nordic seas area. J Clim 26(9):2957–2975. https://doi.org/10.1175/JCLI-D-11-00594.1

Schlichtholz P (2014) Local wintertime tropospheric response to oceanic heat anomalies in the Nordic Seas area. J Clim 27(23):8686–8706. https://doi.org/10.1175/JCLI-D-13-00763.1

Schlichtholz P (2016) Empirical relationships between summertime oceanic heat anomalies in the Nordic seas and large-scale atmospheric circulation in the following winter. Clim Dyn 47(5):1735–1753. https://doi.org/10.1007/s00382-015-2930-5

Schlichtholz P (2019) Subsurface ocean flywheel of coupled climate variability in the Barents Sea hotspot of global warming. Sci Rep 9(1):13692. https://doi.org/10.1038/s41598-019-49965-6

Schlichtholz P (2021) Relationships between wintertime sea ice cover in the Barents Sea and ocean temperature anomalies in the era of satellite observations. J Clim 34(5):1565–1586. https://doi.org/10.1175/JCLI-D-20-0022.1

Schlichtholz P, Houssais MN (2011) Forcing of oceanic heat anomalies by air-sea interactions in the Nordic Seas area. J Geophys Res 116:C01006. https://doi.org/10.1029/2009JC005944

Screen JA, Francis JA (2016) Contribution of sea-ice loss to Arctic amplification is regulated by Pacific Ocean decadal variability. Nat Clim Change. https://doi.org/10.1038/nclimate3011

Screen JA, Simmonds I (2010) Increasing fall-winter energy loss from the Arctic Ocean and its role in Arctic temperature amplification. Geophys Res Lett 37(16):1–5. https://doi.org/10.1029/2010GL044136

Semenov VA, Latif M (2015) Nonlinear winter atmospheric circulation response to Arctic sea ice concentration anomalies for different periods during 1966–2012. Environ Res Lett 10(5):054020. https://doi.org/10.1088/1748-9326/10/5/054020

Serreze MC, Barry RG (2011) Processes and impacts of Arctic amplification: a research synthesis. Glob Planet Change 77(1):85–96. https://doi.org/10.1016/j.gloplacha.2011.03.004

Shu Q, Wang Q, Årthun M, Wang S, Song Z, Zhang M, Qiao F (2022) Arctic Ocean Amplification in a warming climate in CMIP6 models. Sci Adv 8(30):eabn9755. https://doi.org/10.1126/sciadv.abn9755

Simmonds I, Govekar PD (2014) What are the physical links between Arctic sea ice loss and Eurasian winter climate? Environ Res Lett 9(10):101003. https://doi.org/10.1088/1748-9326/9/10/101003

Simmonds I, Li M (2021) Trends and variability in polar sea ice, global atmospheric circulations, and baroclinicity. Ann N Y Acad Sci 1504(1):167–186. https://doi.org/10.1111/nyas.14673

Simon A, Gastineau G, Frankignoul C, Lapin V, Ortega P (2022) Pacific Decadal Oscillation modulates the Arctic sea-ice loss influence on the mid-latitude atmospheric circulation in winter. Weather Clim Dyn 3:1–30. https://doi.org/10.5194/egusphere-2022-69

Skagseth Ø (2008) Recirculation of Atlantic Water in the western Barents Sea. Geophys Res Lett 35:L11606. https://doi.org/10.1029/2008GL033785

Skagseth Ø, Eldevik T, Årthun M, Asbjørnsen H, Lien VS, Smedsrud LH (2020) Reduced efficiency of the Barents Sea cooling machine. Nat Clim Change. https://doi.org/10.1038/s41558-020-0772-6

Smedsrud LH, Ingvaldsen R, Nilsen JEØ, Skagseth Ø (2010) Heat in the Barents Sea: transport, storage, and surface fluxes. Ocean Sci 6(1):219–234. https://doi.org/10.5194/os-6-219-2010

Smedsrud LH, Esau I, Ingvaldsen RB, Eldevik T, Haugan PM, Li C, Lien VS, Olsen A, Omar AM, Otterå OH, Risebrobakken B (2013) The role of the Barents Sea in the Arctic climate system. Rev Geophys 51:415–449. https://doi.org/10.1002/rog.20017

Sorokina SA, Li C, Wettstein JJ, Kvamstø NG (2016) Observed atmospheric coupling between Barents Sea ice and the Warm-Arctic Cold-Siberian anomaly pattern. J Clim 29(2):495–511. https://doi.org/10.1175/JCLI-D-15-0046.1

Sung MK, Kim SH, Kim BM, Choi YS (2018) Interdecadal variability of the warm Arctic and cold Eurasia pattern and its North Atlantic origin. J Clim 31(15):5793–5810. https://doi.org/10.1175/JCLI-D-17-0562.1

Tyrlis E, Bader J, Manzini E, Ukita J, Nakamura H, Matei D (2020) On the role of Ural Blocking in driving the Warm Arctic-Cold Siberia pattern. Q J R Meteorol Soc 146(730):2138–2153. https://doi.org/10.1002/qj.3784

von Storch H, Zwiers FW (1999) Statistical analysis in climate research. Cambr. Univ. Press, London

Walczowski W, Beszczynska-Möller A, Wieczorek P, Merchel M, Grynczel A (2017) Oceanographic observations in the Nordic Sea and Fram Strait in 2016 under the IO PAN long-term monitoring program AREX. Oceanologia 59(2):187–194. https://doi.org/10.1016/j.oceano.2016.12.003

Wang S, Nath D, Chen W, Ma T (2020) CMIP5 model simulations of warm Arctic-cold Eurasia pattern in winter surface air temperature anomalies. Clim Dyn 54:4499–4513. https://doi.org/10.1007/s00382-020-05241-2

Wherry RJ (1931) A new formula for predicting the shrinkage of the coefficient of multiple correlation. Ann Math Stat 2:440–457. https://doi.org/10.1214/aoms/1177732951

Woo SH, Sung MK, Son SW, Kug JS (2015) Connection between weak stratospheric vortex events and the Pacific Decadal Oscillation. Clim Dyn 45:3481–3492. https://doi.org/10.1007/s00382-015-2551-z

Woods C, Caballero R (2016) The role of moist intrusions in winter Arctic warming and sea ice decline. J Clim 29(12):4473–4485. https://doi.org/10.1175/JCLI-D-15-0773.1

Xu X, He S, Li F, Wang H (2018) Impact of northern Eurasian snow cover in autumn on the warm Arctic-cold Eurasia pattern during the following January and its linkage to stationary planetary waves. Clim Dyn 50:1993–2006. https://doi.org/10.1007/s00382-017-3732-8

Xu X, He S, Gao Y, Furevik T, Wang H, Li F, Ogawa F (2019) Strengthened linkage between midlatitudes and Arctic in boreal winter. Clim Dyn 53:3971–3983. https://doi.org/10.1007/s00382-019-04764-7

Yao Y, Luo D, Dai A, Simmonds I (2017) Increased quasi stationarity and persistence of winter Ural blocking and Eurasian extreme cold events in response to Arctic warming. Part I: insights from observational analyses. J Clim 30(10):3549–3568. https://doi.org/10.1175/JCLI-D-16-0261.1

Ye K, Messori G (2020) Two leading modes of wintertime atmospheric circulation drive the recent warm Arctic-Cold Eurasia temperature pattern. J Clim 33(13):5565–5587. https://doi.org/10.1175/JCLI-D-19-0403.1

Zhang R, Screen JA (2021) Diverse Eurasian winter temperature responses to Barents-Kara Sea ice anomalies of different magnitudes and seasonality. Geophys Res Lett 48(13):e2021GL092726. https://doi.org/10.1029/2021GL092726

Zhang P, Wu Y, Simpson IR, Smith KL, Zhang X, De B, Callaghan P (2018) A stratospheric pathway linking a colder Siberia to Barents-Kara Sea sea ice loss. Sci Adv. https://doi.org/10.1126/sciadv.aat6025

Zhao L, Dong W, Dong X, Nie S, Shen X, Xiao Z (2022) Relations of enhanced high-latitude concurrent blockings with recent warm Arctic-Cold continent patterns. J Geophys Res: Atmos 127(16):e2021JD036117. https://doi.org/10.1029/2021JD036117

Zhao L, Liu Y, Ding Y, Li Q, Dong W, Shen X, Cheng W, Yao H, Xiao Z (2023) The Warm Arctic-Cold Eurasia pattern and its key region in winter in CMIP6 model simulations. Adv Atmos Sci. https://doi.org/10.1007/s00376-022-2201-4

Zhuo W, Yao Y, Luo D, Simmonds I, Huang F (2023) The key atmospheric drivers linking regional Arctic amplification with East Asian cold extremes. Atmos Res 283:106557. https://doi.org/10.1016/j.atmosres.2022.106557